

Interdecadal variability in a hybrid coupled
ocean–atmosphere–sea-ice model

S. Kravtsov¹ and M. Ghil²

Department of Atmospheric Sciences and
Institute of Geophysics and Planetary Physics
University of California, Los Angeles

J. Phys. Oceanogr., accepted

January 23, 2004

¹*Corresponding author address:* Dr. Sergey Kravtsov, Department of Atmospheric Sciences and Institute of Geophysics and Planetary Physics, University of California, Los Angeles, 405 Hilgard Ave., Los Angeles, CA 90095-1565. E-mail: sergey@atmos.ucla.edu

²*Additional affiliation:* Département Terre–Atmosphère–Océan and Laboratoire de Météorologie Dynamique, Ecole Normale Supérieure, Paris

Abstract

We study interdecadal climate variability in an idealized coupled ocean–atmosphere–sea-ice model. The ocean component is a fully three-dimensional primitive-equation model and the atmospheric component is a two-dimensional (2-D) energy balance model of Budyko-Sellers-North type, while sea ice is represented by a 2-D thermodynamic model. In a wide range of parameters the model climatology resembles certain aspects of observed climate.

Two types of interdecadal variability are found. The first one is characterized by northward-propagating upper-ocean temperature anomalies in the northwestern part of the ocean basin, and a westward-propagating, wave-like temperature pattern at depth. The other type has larger-scale temperature anomalies that propagate westward in both the upper and deep ocean, along the sea-ice edge. Both types of oscillations have been found previously in similar models that do not include sea ice. Therefore, the oscillation mechanism does not depend on sea-ice feedbacks, nor is it modified very much by the inclusion of sea ice.

For some parameter values, the interdecadal oscillations are self-sustained, while for others they are damped. Stochastic-forcing experiments show that, in the latter case, significant interdecadal signals can still be identified in the time series of oceanic heat transport. The periods of these signals, however, do not closely match those identified in a stability analysis of the deterministic model, when linearized about its steady state. We show that linearization around the actual climatology of the stochastically forced integrations provides a better match for some of the modes that were poorly explained when linearizing about the deterministic model’s steady state. The main difference between the two basic states is in the distribution of climatological convective depth, which is affected strongly by intermittent atmospheric forcing.

1. Introduction

a. Motivation

An important goal of climate research is to identify and understand modes of climate variability on various time scales, in order to interpret past climate changes and anticipate likely variations in future climate (National Research Council 1995). For these purposes, it is useful to distinguish between natural and forced modes of climate variability (Ghil 2002). Ghil and Vautard (1991) have noted the importance of removing the interdecadal signal from the global temperature record to assess the global warming rate (see also Moron et al. 1998).

Kushnir (1994), using multi-year averages of North Atlantic marine observations, has pointed out connections between atmospheric sea-level pressure (SLP) and sea-surface temperature (SST) on interdecadal time scales of roughly 40 years. Deep-ocean expressions of Kushnir's patterns have been described by Levitus (1989a,b) and Greatbatch et al. (1991). Kushnir (1994) argued that the North Atlantic SST anomalies on interdecadal time scales are, if anything, damped by the atmosphere. Thus, decade-long persistence of SST anomalies appears to be due to oceanic processes.

Delworth et al. (1993) have found an interdecadal oscillation similar to that observed by Kushnir (1994) in a global general circulation model (GCM). More recently, Delworth and Mann (2000) have suggested an explanation for Kushnir's observations, which involved an internal oceanic mode energized by the atmospheric variability. Häkkinen (1999, 2000) found evidence for nonlocal responses of the North Atlantic's thermohaline circulation (THC) to the atmospheric variability and suggested that these trends are manifestations of a coupled decadal cycle. The type of behavior found by Delworth and Mann (2000) and Häkkinen (1999, 2000) was not found in the coupled ocean-atmosphere model of Saravanan et al. (2000). The main physical difference between these models is that the latter did not include sea ice, to which the THC is known to be sensitive (see below).

A good way to approach climate problems in general is through a hierarchy of climate models (Panel on Climate Variability 1998; Ghil and Robertson 2000, and references there). Coupled, highly resolved GCMs are known to produce behavior as complex as the climate

system itself, and their interpretation is often just as difficult. The simplest process models, on the other hand, allow one to explore fully certain conceptual aspects of climate evolution, but their results are hard to relate directly to observations. Climate models of intermediate complexity provide a bridge between the conceptual understanding achieved through simple models and the numerous phenomena modeled by detailed GCMs.

Interdecadal climate oscillations have been found in a variety of intermediate, three-dimensional (3-D) THC models (see below). Interactions between the THC and sea ice on interdecadal time scales, however, have been less well studied. The purpose of this paper is to document interdecadal variability in a THC model that includes a sea-ice component.

b. Background

1) IDEALIZED THC MODELS

Standard tools to study THC variability have been 3-D coarse-resolution models in a box geometry. Depending on model parameters and surface forcing, such models exhibit various kinds of decadal-to-interdecadal variability.

(i) *Sensitivity to surface boundary conditions.* The THC is known to be sensitive to an ocean model's upper boundary conditions. In a series of papers, Weaver and collaborators studied in detail oscillations that arise when using the so-called mixed boundary conditions, that is, a restoring condition for SST and a fixed virtual salt flux condition (Weaver and Sarachik 1991a,b; Weaver et al. 1991, 1993; Weaver 1995). They concluded that the system's variability depends on the magnitude and spatial structure of the surface salinity forcing specified.

Chen and Ghil (1995) found two types of decadal-scale oscillations in a similar model (see also Greatbatch and Zhang 1995) and plotted their dependence on the intensity of the surface fluxes of mass, momentum and heat. They showed that the model's behavior only depends on certain broad characteristics of the virtual salt flux's spatial distribution. They also detected an interesting oscillation-permitting regime in a constant-salinity version of their model forced with a heat flux that is fixed in time. The oscillation's spatial and temporal characteristics were similar to those found in the more highly resolved, global ocean-atmosphere GCM of Delworth et al. (1993) and Delworth and Mann (2000).

(ii) *Oscillations in models with fixed-flux and EBM boundary conditions.* Fixed-flux boundary conditions have been shown to generally stabilize the THC relative to the mixed boundary condition case (Zhang et al. 1993; Greatbatch and Zhang 1995; Cai et al. 1995; Cai 1995, 1996; Capotondi and Saravanan 1996). Molemaker and McWilliams (2003), studying the bifurcation properties of the THC in a sectorial basin, pointed to different physical mechanisms that participate in the oscillations under mixed and fixed-flux boundary conditions.

A more physically appealing condition compared to either mixed or fixed-flux boundary conditions is to use a simple diagnostic energy-balance model (EBM: Budyko 1969; Sellers 1969; North et al. 1981) of the atmosphere. Models that couple detailed prognostic components to simple diagnostic modules are often called hybrid models (Neelin et al. 1994; Ghil and Robertson 2000). Chen and Ghil (1996) have shown that the oscillations found by Chen and Ghil (1995) are retained in the presence of such coupling (see also Pierce et al. 1996; Huck et al. 2001) and computed bifurcation and regime diagrams for such a coupled model's behavior. A further step towards physical realism was taken by adding an interactive hydrological cycle to the diagnostic atmospheric component of the model (Chen 1995, Ch. 4).

Huck et al. (1999) have carried out an extensive analysis of the interdecadal oscillations forced by constant surface fluxes and found two types of oscillations. One of them involved stationary temperature anomalies in the northwestern corner of the ocean basin, similar to those documented by Chen and Ghil (1995, 1996) and Greatbatch and Zhang (1995). The second type was characterized by temperature anomalies that propagate westward along the northern boundary of the model ocean.

Te Raa and Dijkstra (2001) reproduced the oscillations of the second type and explained their physical mechanism. The details of the physical mechanism for the first type of oscillation are not fully understood. Colin de Verdière and Huck (1999) and Huck et al. (1999) suggested that long waves, which exhibit a baroclinic energy conversion cycle and feed on the mean stratification, play a crucial role in both types of oscillation and set the oscillation period.

A number of studies have noted the sensitivity of the interdecadal THC modes to various subgrid parameters (Huck et al. 1999), to bottom topography (Greatbatch et al. 1997; Winton 1997), to wind stress forcing (Chen and Ghil 1995; Huck et al. 2001), and to model resolution (Fanning and Weaver 1998). Still, for a wide range of the relevant model parameters, this

interdecadal oscillation is quite robust.

(iii) *Stochastic excitation of THC modes.* Chen and Ghil (1996) have shown that the interdecadal oscillation in their model arises by an oscillatory instability that leads to a Hopf bifurcation (Ghil and Childress 1987, section 12.4; Huck and Vallis 2001; Te Raa and Dijkstra 2001). In a subcritical regime, that is, below the Hopf bifurcation point, the interdecadal oscillation is damped at constant forcing, but it can reemerge when stochastic atmospheric forcing is applied (Griffies and Tziperman 1995; Delworth and Greatbatch 2000). Therefore, even in the subcritical regime, the same THC dynamics might be operative in producing potentially predictable climate signals, provided the associated THC mode is not too strongly damped (cf. Delworth and Mann 2000).

2) COUPLING TO SEA ICE

Modeling experience (Kravtsov 1998, 2000; Jayne and Marotzke 1999; Kravtsov and Dewar 2003; Gildor and Tziperman 2000, 2001) shows that the THC is particularly sensitive to the way in which sea-ice processes are represented in the model. Important sea-ice effects include: (i) the albedo effect associated with a positive feedback between the high albedo of sea ice and reflected solar radiation; (ii) the insulation effect due to low sea-ice conductivity, which is inversely proportional to the sea-ice thickness; (iii) the phase-transition effect, which anchors the surface water temperature underneath the sea ice to be near the freezing point; and (iv) the effect of brine rejection, or freshwater input, which modifies the surface boundary condition as the ice forms or melts. The simplest sea-ice representation used in coupled ocean-atmosphere models that possesses all the important properties identified above is the so-called thermodynamic sea-ice model (Semtner 1976).

This model has been widely used in climate studies (Willmott and Mysak 1989; Yang and Neelin 1993, 1997; Zhang et al. 1995; Lohmann and Gerdes 1998; Kravtsov 1998, 2000; Kravtsov and Dewar 2003). Zhang et al. (1995) have argued that their model's oscillations are due to the insulating effect of sea ice, which creates density imbalances at the surface (cf. Cai 1995). The 3-D structure of the oscillation is, however, similar to that found in the no-ice model by Yin and Sarachik (1995). Different types of interannual-to-interdecadal variability have been found in a hybrid coupled model with sea ice by Chen (1995, Ch. 5) and Chen and Ghil (1997, unpublished manuscript). These highly nonlinear, relaxation-type oscillations

occurred at lower levels of imposed upper-boundary fluxes than the oscillations found previously in the same model without sea ice (Chen and Ghil 1995, 1996), thus indicating a large model sensitivity to sea-ice processes. Yang and Neelin (1993, 1997) documented yet another type of the sea-ice-related oscillations. In their work, it was the brine rejection effect that was most important for the model’s behavior.

c. Present approach

Combining a 3-D ocean model with an EBM for the atmospheric component and a thermodynamic sea-ice model (Chen 1995, Ch. 5; Lohmann and Gerdes 1998) is both simple and natural in order to study interactions of sea ice with interdecadal ocean modes. Given our primary interest in the sea-ice effects on the model’s interdecadal variability, we perform sensitivity studies by varying sea-ice-related parameters, as well as those oceanic parameters that are likely to affect sea-ice dynamics, over a wide range. All other parameters are kept fixed at the values that appear to be most reasonable.

The model is described in section 2. In sections 3 and 4, we discuss the parameter sensitivity of the modeled climatology and self-sustained oscillations, respectively. Section 5 deals with the linear stability analysis of the model when the oscillations are damped. The stochastic-forcing experiments in section 6 reveal discrepancies between the periods of their leading oscillatory modes and those expected from stability analysis about the deterministic model’s steady state. Stability analysis of the coupled model linearized around the stochastic-run climatology yields, in many cases, the numerically obtained periods. Concluding remarks follow in section 7.

2. Model formulation

a. Model geometry and grids

The ocean model consists of a single rectangular basin on a β -plane, in cartesian (x, y, z) coordinates. This ocean basin is 6400-km wide and occupies $f_W = 1/4$ of the globe, while land occupies the remaining $f_L = 1 - f_W = 3/4$. Our ocean basin is, therefore, wider than the Atlantic and narrower than the Pacific. Such a choice is an attempt to model the global

oceanic contribution to the overall energy budget of the Earth. Both the ocean and the land extend from the equator, $Y_S = 0$, to $Y_N = 9600$ km ($\approx 86^\circ\text{N}$).

The choice of cartesian geometry is motivated by the ease of coupling between the atmospheric component and the oceanic one in this geometry. We will show that the center of action of interdecadal variability in the model is situated south of the time-mean ice-edge position, that is, south of roughly 70°N in most cases, so the use of cartesian geometry does not distort qualitative aspects of this behavior (see also Huck et al. 1999). The model’s atmospheric channel overlies the ocean and the land; periodic boundary conditions are assumed in the x -direction. The ocean’s depth is $h_o=4000$ m, and the atmospheric height is $h_a=10$ km.

The governing equations are discretized on a rectangular grid of 400 km \times 400 km \times 15 levels or, equivalently, of $3.6^\circ \times 3.6^\circ \times 15$ levels. Vertical grid spacing is exponentially increasing from 50 m near the surface to 742 m near the bottom.

b. Governing equations

1) OCEANIC COMPONENT

The ocean component is a 3-D primitive-equation model that uses the hydrostatic and Boussinesq approximations. It is similar to the GFDL MOM model (Pacanowski 1996) on a beta-plane, with $\beta = 2 \times 10^{-11} \text{ m}^{-1}\text{s}^{-1}$, and vertical and horizontal viscosities $A_H = 2 \times 10^5 \text{ m}^2\text{s}^{-1}$ and $A_V = 10^{-4} \text{ m}^2\text{s}^{-1}$, respectively. The equation of state is linear and uses the thermal expansion coefficient $\alpha = 2 \times 10^{-4} \text{ C}^{-1}$, while salinity variations are neglected in the model. The advection–diffusion equation for the ocean temperature uses a horizontal diffusivity of $K_H = 10^3 \text{ m}^2\text{s}^{-1}$ and two distinct values for the vertical diffusivity K_V , which are listed in Table 1. A standard convective adjustment scheme is applied to guarantee the complete removal of static instabilities.

Table 1

The boundary conditions on the lateral walls and the bottom of the ocean are no-flux for temperature and no-slip for velocities, except for the equatorial boundary, where reflection conditions are used. The wind-stress forcing in our model is assumed constant in time and has no meridional component; the zonal component τ_0^x is taken from Bryan (1987). Sea ice reduces the wind stress exerted upon the ocean surface; hence, in its presence, an exponential transfer

function is used to model this stress (Willmott and Mysak 1989):

$$\tau^x = \tau_0^x \exp(-h), \quad (1)$$

where h is the sea-ice thickness expressed in meters.

The surface boundary condition for temperature is

$$K_V \frac{\partial T}{\partial z} = \frac{H_{s,o}}{\rho_0 c_p}; \quad (2)$$

here $\rho_0 = 1000 \text{ kg m}^{-3}$ and $c_p = 4000 \text{ J kg}^{-1} \text{C}^{-1}$ are the density and heat capacity of water, respectively, and $H_{s,o}$ is heat flux into the ocean.

2) ATMOSPHERIC COMPONENT

We employ a 2-D EBM (Budyko 1969; Sellers 1969; North et al. 1981) as the atmospheric component in the coupled model, following Chen (1995, Ch. 3) and Chen and Ghil (1996). The atmospheric model is purely diagnostic, since we neglect atmospheric thermal inertia. The atmosphere is assumed to be transparent to shortwave radiation R , absorb the back radiation O from the ocean and sea ice, emit longwave radiation both upward and downward with intensity B , and exchange sensible and latent heat H_{SL} with the ocean and sea ice.

The atmospheric heat budget at equilibrium is given by

$$R - B - H_s - \nabla \cdot F_h = 0, \quad (3a)$$

where H_s is the net downward heat flux at the bottom of the atmosphere and F_h is the atmospheric heat transport. Over the ocean and sea ice, H_s given by

$$H_s = R + B - O - H_{SL}, \quad (3b)$$

while the insulating boundary condition at the atmosphere–land boundary requires that, over land,

$$H_s = 0. \quad (3c)$$

Net shortwave radiation R at the top of the atmosphere equals

$$R = Q(1 - a); \quad (4)$$

here Q is time-averaged solar radiation flux and a is planetary albedo: Q is given, in W m^{-2} and as a function of latitude ϕ , by

$$Q = \frac{1355}{4} [1 - 0.241(3 \sin^2 \phi - 1)], \quad (5)$$

while albedo is nondimensional and is given by

$$a = 0.3 + 0.07(3 \sin^2 \phi - 1) + \Delta a \text{ sign}(h). \quad (6)$$

In Eq. (6), Δa is the parameter that controls the strength of ice–albedo feedback (Wang and Stone 1980). In our experiments, we will use several values of this parameter, listed in Table 1. The net radiative forcing given by Eqs. (4)–(6) is a reasonable approximation to the observed distribution (Stephens et al. 1981).

The atmospheric longwave radiation is parameterized as

$$B = B_0 + B_t T_a, \quad (7)$$

with $B_0 = 183 \text{ W m}^{-2}$ and $B_t = 1.63 \text{ W m}^{-2} \text{ C}^{-1}$, and with the atmospheric temperature T_a in degrees C (Budyko 1969; North et al. 1981). A similar linear approximation for oceanic back radiation is used:

$$O = \sigma_B T_r^4 + 4\sigma_B T_r^3 T_s; \quad (8)$$

here $T_r = 273 \text{ K}$ is a reference temperature, $\sigma_B = 5.7 \times 10^{-8} \text{ W K}^{-4}$ is the Boltzmann constant, and T_s , in degrees C, is the temperature of the ocean or sea-ice surface.

The sensible and latent heat exchange is given by

$$H_{\text{SL}} = K_{\text{O-A}}(T_s - T_a), \quad (9a)$$

with $K_{\text{O-A}} = 30 \text{ W m}^{-2} \text{ C}^{-1}$ (Haney 1971) in the ocean region, and

$$H_{\text{SL}} = K_{\text{A-I}}(T_s - T_a) \quad (9b)$$

in the sea-ice region. The parameter $K_{\text{A-I}}$ will be one of the control parameters in our integrations and the values we use are listed in Table 1.

We parameterize the atmospheric heat transport as

$$F_h = -c_p a \rho_a h_a D \nabla T_a, \quad (10)$$

where $c_{p,a} = 1000 \text{ J kg}^{-1}\text{C}^{-1}$ is the atmospheric heat capacity and $\rho_a = 1.27 \text{ kg m}^{-3}$ is a representative atmospheric density. The atmospheric diffusivity D will also be used as one of the control parameters, following Chen and Ghil (1996) and Ghil (2001); the values we use are listed in Table 1. Lateral boundary conditions for the atmospheric model are

$$F_h = 0 \quad (11)$$

along the northern and southern boundaries.

3) SEA-ICE COMPONENT

The evolution of sea-ice thickness h is governed by

$$\rho_i L_f \frac{\partial h}{\partial t} = H_{s,o} - H_s + K_H \rho_i L_f \nabla^2 h; \quad (12)$$

here $\rho_i L_f = 2.72 \times 10^8 \text{ J m}^{-3}$ (Bryan 1969; Maykut 1986). The meridional gradient of sea-ice thickness is set to zero at the northern boundary of the model's ocean basin.

The sea-ice surface temperature is determined by

$$T_s = \frac{h}{k_i} H_s + T_f, \quad (13)$$

where $T_f = -1.9 \text{ C}$ is the freezing temperature of sea water, and we use the value $k_i = 2.17 \text{ W m}^{-1}\text{C}^{-1}$ for sea-ice conductivity (Semtner 1976). At the sea-ice surface, T_s cannot exceed the freezing point of fresh water, of 0 C : if it does, T_s is reset to zero and the resulting heat imbalance is used to melt sea ice (Bryan 1969).

4) COUPLING

The components are coupled by assigning

$$H_{s,o} = H_s, \quad h = 0, \quad (14a)$$

$$H_{s,o} = K_{O-I}(T_f - T_{s,o}), \quad h > 0, \quad (14b)$$

in the ice-free and ice-covered regions, respectively, where $T_{s,o}$ is sea-surface temperature under sea-ice. We will see in the next sections that the parameter K_{O-I} that governs the strength of sea-ice–ocean coupling is one of the most important model parameters.

In solving Eq. (12), we use Eq. (14b) at every point, and then set negative sea-ice thickness values to zero; the resulting heat imbalance is used, in this case, to warm the ocean's upper

layer. The ocean model is forced by the full Eqs. (13a,b), and the new atmospheric temperature and sea-ice-surface temperature are computed by solving Eqs. (2–10) and Eq. (13) with newly determined sea-ice thickness and sea-surface temperature values.

c. Numerical implementation

The equations above are rewritten in conservative form and discretized on a B-grid (Arakawa 1966) using second-order-accurate centered differences. In the momentum equations, explicit and semi-implicit operators are used for vertical and horizontal friction terms, respectively, along with a fully implicit Coriolis term. The barotropic velocity is obtained via integration of the barotropic vorticity equation written in terms of the barotropic streamfunction. The resulting elliptic equation has nonconstant coefficients, due to the implicit Coriolis term; in solving it, a 9-point stencil is used for the Laplacian operator to suppress a checker-board numerical mode. The tracer equations are explicit, except in the numerical implementation of the surface heat-flux parameterization below the sea ice, Eq. (14b), where an implicit representation of $T_{s,o}$ is used. All elliptic problems with nonconstant coefficients are inverted using successive overrelaxation.

The system is integrated forward using a fourth-order Runge-Kutta method with a time step of 1.825 days (200 time steps per year). Double-resolution simulations were performed in several cases and have shown that our model’s behavior is insensitive to horizontal resolution.

3. Time-mean states

Since we are primarily interested in the sea-ice effects on our model’s variability, we will vary the sea-ice-related parameters introduced above: the albedo parameter Δa , the atmosphere–sea-ice coupling coefficient K_{A-I} , and the ocean–sea-ice coupling coefficient K_{O-I} . Additional parameters we will vary are the vertical diffusivity of heat K_V in the ocean, which affects strongly the modeled THC variability and the atmospheric diffusivity D that controls the atmospheric heat transport. In addition to its effect on the presence or absence of interdecadal THC oscillations in Chen and Ghil’s (1996) model, D turns out here to have a strong effect on the sea-ice edge location.

The selected parameter values we use are listed in Table 1, and we explored each of their possible combinations. The parameter values that produce model climatology most similar to the observed are in bold. In particular, the choice of $\Delta a = 0.1$ results in realistic sea-ice thickness and extent. We only describe below the experiments with this value of Δa . The behavior at $\Delta a = 0$ and $\Delta a = 0.2$ is qualitatively similar to that at $\Delta a = 0.1$.

Maykut (1986) estimated the value of K_{A-I} as $24.2 \text{ W m}^{-2}\text{C}^{-1}$. However, lower values have been used by Willmott and Mysak (1989), Chen (1995), and Chen and Ghil (1997, unpublished manuscript). We will thus explore the behavior with Maykut’s value, as well as higher and lower values, in our experiments.

The most controversial parameter is K_{O-I} : estimates that are based on measured heat-flux values depend on geographic location, time of year, and ocean stratification (Josberger 1987; Wood and Mysak 1989; McPhee 1992). Lenderink and Haarsma (1996) have listed estimates that range from 20 to $200 \text{ W m}^{-2} \text{ C}^{-1}$, while Willmott and Mysak (1989), Yang and Neelin (1993, 1997), Chen (1995), and Chen and Ghil (1997) have used even lower values, on the order of a few units, for this coefficient. Although we think that higher values are more realistic, we explored a wide range of K_{O-I} values (see Table 1).

For each set of parameter values, the model was spun up for 5000 years, followed by an additional 2000-year-long integration. The climatological characteristics obtained from the latter 2000 years will now be discussed, for several simulations.

a. Climatology

We arbitrarily choose the experiment with $K_{O-I} = 15 \text{ W m}^{-2} \text{ C}^{-1}$, $K_{A-I} = 24.2 \text{ W m}^{-2} \text{ C}^{-1}$, $K_V = 1.0 \times 10^{-4} \text{ m}^2 \text{ s}^{-1}$, and $D = 2 \times 10^6 \text{ m}^2 \text{ s}^{-1}$ and now describe its time-mean climate. Other experiments have similar qualitative features.

1) ATMOSPHERIC AND SEA-ICE STATES

The atmospheric temperature and sea-ice thickness are plotted in Figs. 1a,b. The meridional atmospheric temperature gradient [panel (a)] is steepest in the land regions, due to the land’s lack of thermal capacity. In the ocean region, the heat is partially transported by the oceanic currents, so that the meridional heat transport by the atmosphere is smaller. There is

Fig. 1

a slight zonal dependence in the atmospheric temperature field over the ocean, which is similar to that in the sea-ice thickness distribution [panel (b)]. The sea ice has a reasonable extent and a maximum thickness of about 3 m.

2) OCEAN STATE

The oceanic zonally averaged climatology is shown in Figs. 1c,d. A clear 1000-m-thick thermocline is seen in the temperature distribution [panel (c)], while the meridional overturning streamfunction [panel (d)] has a two-cell structure. The two cells have a common sinking branch located in a narrow region near the sea-ice edge. The main cell is characterized by broad upwelling equatorward of the sea-ice edge, and poleward surface flow; a weaker opposite cell is found under the sea ice. The maximum of the overturning streamfunction is located at approximately 60 N and at the depth of 1000 m, that is at the bottom of the main thermocline.

b. Changes in model states subject to varying parameters

1) ATMOSPHERIC AND SEA-ICE STATES

The sea-ice climatological characteristics are plotted against K_{O-I} in Fig. 2: the mean sea-ice thickness in panel (a), and the sea-ice-edge latitude in panel (b). Different symbols and line types are used to illustrate dependence on other control parameters. In general, as K_{O-I} increases, the sea ice becomes thicker but smaller in meridional extent, while it grows in both thickness and extent with decreasing D and K_V ; the dependence on K_{A-I} is weak.

Fig. 2

2) OCEANIC-STATE CHANGES

The meridional overturning Ψ_m generally increases with K_{O-I} and K_V , and decreases with increasing D , ranging from about 18 to 33 Sv for different parameter values, while the dependence on K_{A-I} is, once again, weak (not shown). The changes in overturning are accompanied by those in oceanic heat transport H_O . The mutual dependence between the latter and the atmospheric heat transport H_A is shown in Fig. 3.

Fig. 3

The values of atmospheric transport that our model produces are on the order of 4–5 PW, while the oceanic transport is of about 1 PW. Observations at 24 N show that total poleward heat transport in the Atlantic is 1.2 ± 0.3 PW (Hall and Bryden 1982) and in the Pacific 0.76 ± 0.3 PW (Bryden et al. 1991). The implied global oceanic heat transport value of $1.96 \pm$

0.6 PW is consistent with a more recent, but lower, estimate of 1.5 ± 0.3 PW by Macdonald and Wunsch (1996). Trenberth and Caron (2001) estimate the annual mean poleward atmospheric heat transport in the Northern Hemisphere to be 5.0 ± 0.14 PW and the global oceanic heat transport to be just 20% of the total, which gives an estimate of about 1.25 PW for the latter. Thus, our model’s transports are generally consistent with the observational estimates and slightly on the lower side, provided that our ocean basin is thought of as representing the global Northern Hemisphere ocean.

In summary, the variations in model parameters produce a continuous range of qualitatively similar climatological states, which differ, however, in several quantitative measures of the Earth’s “heat-engine efficiency.” The model climate depends most strongly on the ocean–sea-ice coupling coefficient K_{O-I} , while dependence on the atmosphere–sea-ice coupling coefficient K_{A-I} is much weaker.

4. Intrinsic variability

The model possesses intrinsic variability at the two lower values of the ocean–sea-ice coupling coefficient we use, $K_{O-I} = 5$ and $15 \text{ W m}^{-2}\text{C}^{-1}$. Two types of variability occur: interannual variability is characterized by variations localized in the sea-ice region and having but little effect on the larger-scale ocean circulation. In this paper, we do not examine these localized variations further and concentrate on interdecadal variability, which arises as a basin-wide, self-sustained oscillation only in the experiments with $K_{O-I} = 5 \text{ W m}^{-2}\text{C}^{-1}$ and $K_V = 10^{-4} \text{ m}^2\text{s}^{-1}$. Lower values of D or of K_{O-A} would probably extend the range of K_{O-I} over which such variability is obtained (see Chen and Ghil 1996; Ghil 2001) but we did not deem the parameter dependence in question to require further investigation at this point.

Time series of several global quantities during the 71-year oscillation obtained with $K_{A-I} = 24.2 \text{ W m}^{-2}\text{C}^{-1}$ and $D = 2 \times 10^6 \text{ m}^2\text{s}^{-1}$ are plotted in Fig. 4. To filter out signatures of the accompanying interannual signal, we have constructed a composite of the interdecadal oscillation by averaging over many cycles. The time series of the maximum meridional overturning is shown in panel (a). The oscillation is slightly asymmetric, with a faster increase and slower decrease in the overturning. In panel (b) we plot, following Huck et al. (1999) and Te Raa and

Fig. 4

Dijkstra (2002), the time series of quantities ΔT_{E-W} and ΔT_{N-S} , which are the horizontally and depth-averaged differences between eastern and western, and northern and southern boundary temperatures in the upper, 1000 m thick ocean layer, respectively. The two time series are out of phase, with ΔT_{E-W} leading and ΔT_{N-S} lagging the maximum overturning by roughly a quarter of the oscillation period; the two temperature gradients are thus in phase opposition in this interdecadal oscillation, which we call of Type I. Huck et al. (1999, Fig. 13) observed a similar phase lag in a model without sea ice, forced by a heat flux that was constant in time.

The spatio-temporal pattern of this oscillation of Type I resembles the one found by Chen and Ghil (1995, 1996), Greatbatch and Zhang (1995), and Huck et al. (1999) in models without sea ice, either forced by a heat flux that is kept constant in time or coupled to simple EBMs. The evolution of zonally averaged fields is shown in Fig. 5.

Fig. 5

The anomalies of meridional overturning are plotted on the left and temperature anomalies on the right. At $t = 0$, the negative overturning anomaly fills the basin. One eighth of a period later, a positive anomaly forms near the surface at about 70 N, subsequently grows in size, and eventually fills the basin at $t = 1/2$ of the oscillation period (the same pattern as at $t = 0$, but with the opposite sign), after which the overturning follows the inverse evolution. The temperature anomalies have maximum amplitude in the northern part of the upper ocean. They are characterized by a dipolar structure, whose evolution is consistent with advection of the mean, zonally averaged temperature field by anomalous overturning (left panels). Similar structures have been observed by Greatbatch and Zhang (1995, Fig. 5) and Chen and Ghil (1996, Fig. 6).

Fig. 6

The evolution of depth-averaged temperature anomalies is shown in Fig. 6. The temperature anomalies in the upper-ocean layer (left panels) are localized in the northwestern corner of the basin, and propagate northward, while lower-layer temperature anomalies exhibit some propagation north of 60 N (right panels). The behavior in the upper layer is similar, to some extent, to that in Greatbatch and Zhang (1995, Fig. 6) and Chen and Ghil (1996, Fig. 5), as well as to that in Huck et al. (1999, Fig. 9). Huck and Vallis (2001) found a similar spatio-temporal pattern of interdecadal temperature anomalies.

Chen and Ghil's (1995, 1996) and Greatbatch and Zhang's (1995) SST pattern is characterized by anticlockwise movement of two vortices of opposite sign, while our upper-layer

temperature pattern in Fig. 6 involves northward propagation. This difference might be due to the spherical geometry of the ocean basin used in the above-mentioned studies, in contrast to our β -plane model. It is plausible that kinematic constraints due to the convergence of meridians will lead to an anticlockwise rotation of temperature anomalies, while this effect is absent in rectangular geometry.

We conclude, therefore, that the interdecadal oscillations in our model do not crucially depend on the presence of sea ice, since they closely resemble those found previously in models without sea ice. An experiment in which sea-ice thickness was not allowed to vary (not shown) confirmed this conclusion.

5. Linear stability analysis

For higher values of K_{O-I} no self-sustained interdecadal oscillations are found in our model. This might be due to the high value of the ocean–atmosphere exchange coefficient, $K_{O-A} = 30 \text{ W m}^{-2} \text{ C}^{-1}$, used in our model (Chen and Ghil 1996; Ghil 2001), but it is not a matter of great concern: weakly damped modes are likely to be excited by the stochastic forcing associated with intrinsic atmospheric dynamics (Griffies and Tziperman 1995; Delworth and Greatbatch 2000). To extract the least-damped modes of interdecadal variability, we performed a linear stability analysis of our model equations.

We linearized the model about its climatological state for parameter settings for which the interdecadal oscillation was not self-sustained, but interannual variability was present. Since the latter does not strongly affect much of the basin and has a fairly small amplitude (not shown), the climatological state is close to the true steady state in the absence of large-amplitude interdecadal oscillations.

The linearized operator used in the linear stability analysis includes several approximations: we keep the spatial pattern of the sea ice and the convective distribution constant and neglect the correction to the sea-ice surface temperature described in section 2. Strongly nonlinear effects associated with migrations of sea-ice edge and convective variability were thus neglected. The temperature anomalies in the convecting regions were redistributed uniformly, according to the mean-state convective distribution, that is every convecting column was characterized by

a single temperature value in the approximate linearized operator. In addition, the changes in time of the barotropic velocity were neglected, and prognostic momentum equations replaced by their diagnostic counterparts.

We computed the linearized operator for such an approximate system of equations and extracted its eigenmodes. The results of this eigenmode analysis were compared with those of perturbation experiments, in which we added an arbitrary perturbation of oceanic temperature to the model’s climatological state and recorded the evolution of decaying anomaly fields. In these experiments, we used the full nonlinear equations but extracted the decaying modes at a stage at which the anomalies have a very small amplitude, so that their evolution is essentially linear. After an initial adjustment interval, the time series of all the variables we inspected can be approximated quite well by the product of an exponential decay and a harmonic function in time (not shown). The damping time and the period are the same for all variables and hence the numerical behavior does represent the least-damped linear eigenmode of the system.

Interdecadal modes with the correct period and spatial structure were only obtained when the fixed-distribution convection was included in the approximate linearized operator described above. When computing the interdecadal eigenmodes of a linearized operator that allows temperature anomalies within a convective column to have a vertical structure, rather than treating the column as a single temperature variable, we obtained very different, usually much longer, periods. Huck and Vallis (2001) found similarly large sensitivity to convective adjustment in their model’s interdecadal variability.

The results of the linear eigenmode analysis are summarized in Fig. 7. The periods (left panels) and inverse damping time scales (right panels) of the least-damped interdecadal eigenmode are plotted against K_{O-I} as circles. Panels (a–d) show the results for different values of K_V and D , while scatter within each frame is due to dependence on K_{A-I} . The oscillation period decreases and the oscillation becomes more damped with increasing K_{O-I} . Note that some of the modes turn out to be slightly unstable due to approximations we have made to the linearized operator, whereas in reality they must be damped. All oscillations detected are interdecadal, with periods between 30 and 80 years, and have $\text{Re}(\lambda) > -0.1 \text{ year}^{-1}$. Their harmonic component (not shown) strongly resembles the self-sustained oscillation discussed in the previous section.

Fig. 7

6. Stochastic-forcing experiments

The linear eigenmodes computed above are only weakly damped and are thus likely to be maintained by stochastic forcing. To check this hypothesis, we add a zonally uniform stochastic component $H'_{s,a}(y)$ to Eq. (3b) for the heat flux at the bottom of the atmosphere,

$$H'_{s,a} = H_{s,a}^0 [A(t) \sin(2\pi y/L_y) + B(t) \cos(2\pi y/L_y)]; \quad (15)$$

here L_y is the meridional extent of the ocean basin and $H_{s,a}^0 = 50 \text{ W m}^{-2}$, while A and B are independent Gaussian white-noise random variables (Saravanan and McWilliams 1998). Stochastically forced integrations that are 2000-year long were then performed and analyzed.

a. Singular spectrum analysis (SSA)

Plotted as crosses in the left panels of Fig. 7 are the periods of the leading significant modes. These periods were determined by singular spectrum analysis (SSA: Vautard and Ghil 1989; Dettinger et al. 1995; Ghil et al. 2002) of a model time series. The ocean's maximum meridional heat transport has been chosen for this analysis since it is one of the most important measures of climate variability (Häkkinen 1999). Other time series of global model quantities give very similar results (not shown).

Typical SSA results are presented in Fig. 8 for a stochastically forced integration with $K_{O-I} = 180 \text{ W m}^{-2} \text{ C}^{-1}$, $K_{A-I} = 5 \text{ W m}^{-2} \text{ C}^{-1}$, $K_V = 0.5 \times 10^{-4} \text{ m}^2 \text{ s}^{-1}$, and $D = 2 \times 10^6 \text{ m}^2 \text{ s}^{-1}$. There are two significant oscillatory pairs, with periods of 54 and 83 years; the first of these is dominant. It is the periods of such dominant modes that are plotted as x-symbols in the left panels of Fig. 7. While for some values of the parameters the periods of linear eigenmodes and leading SSA modes match, in a large number of cases they do not. This is particularly noticeable in the experiments with $K_V = 0.5 \times 10^{-4} \text{ m}^2 \text{ s}^{-1}$ (Figs. 7c,d).

The stochastic forcing in Eq. (15) has a large amplitude and might cause large changes in the model's climatology. We now check if the latter changes can explain discrepancies between the oscillation periods predicted by the linear stability analysis of section 5 and those obtained

Fig. 8

in the stochastically forced runs (Fig. 7).

b. Linear stability analysis

We performed a stability analysis, like that in section 5, but linearizing the model about the stochastic-run climatology. The changes in the climatological ocean and sea-ice states due to stochastic forcing are in fact fairly small, except in the distribution of the depth reached by convection. The stochastically forced climatology is characterized, in general, by a reduced convective activity (see Fig. 9); we found that this leads to longer periods of the linear eigenmodes.

Fig. 9

The results of the linear stability analysis with respect to the “stochastic basic state” are plotted in Fig. 7 as open triangles. For a number of parameter settings, these results produce a much better match to those obtained by SSA analysis of the actual stochastically forced simulation than those using the deterministic steady state, especially in cases with small $K_V = 0.5 \times 10^{-4} \text{ m}^2 \text{ s}^{-1}$ (panels c,d). For $K_V = 10^{-4} \text{ m}^2 \text{ s}^{-1}$, some of the SSA modes that are not explained by the linearization around the steady state are matched by the “stochastic basic state” eigenmodes; this is the case, for example, at large values of K_{O-I} (Figs. 7a,b).

Still, neither linearization about the deterministic steady state nor about the “stochastic basic state” explain all of the SSA modes in Fig. 7. The damping times of all “stochastic basic state” eigenmodes, as well as their periods, are in most cases longer than those obtained for the deterministic steady state.

We conclude that the changes in the climatological state due to large-amplitude stochastic forcing are important in modifying the model’s interdecadal variability; this is especially true for the changes in convective activity. The phenomenon of interdecadal variability by itself is, however, robust. The damped interdecadal eigenmodes do become excited by the stochastic forcing and can be detected as significant modes by SSA analysis. The actual periods of interdecadal variability in the stochastically forced model are roughly bracketed, from below and above, by those predicted by the linear stability analyses using the steady state and stochastic

climatology as the basic state, respectively.

c. Structure of eigenmodes

For all sets of parameters, except those with $K_{O-I} = 180 \text{ W m}^{-2} \text{ C}^{-1}$, the linear eigenmodes of the stochastically forced run have spatial signatures similar to those of eigenmodes of the model linearized about the steady state; the latter are, in turn, similar to those of self-sustained oscillation of section 4 (Figs. 4–6). An eigenmode with a different spatial signature arises when $K_{O-I} = 180 \text{ W m}^{-2} \text{ C}^{-1}$.

We present an example of such an oscillation with $K_{A-I} = 5 \text{ W m}^{-2} \text{ C}^{-1}$, $K_V = 0.5 \times 10^{-4} \text{ m}^2 \text{ s}^{-1}$, and $D = 2 \times 10^6 \text{ m}^2 \text{ s}^{-1}$. It has a period of 54 years and an inverse damping time scale of $\text{Re}(\lambda) = -0.08 \text{ year}^{-1}$. This oscillation also appears as the leading significant SSA mode in Fig. 8.

The time series of significant quantities over the oscillation cycle are presented in Fig. 10. This figure is analogous to Fig. 4, but phase relations between the maximum meridional overturning [panel (a)] and the North–South and East–West temperature differences [panel (b)] is quite distinct from those depicted in that figure. In particular, the overturning is in phase opposition with ΔT_{E-W} , which, in turn, leads ΔT_{N-S} by about one quarter of a period. This is a trademark of the interdecadal oscillations described in detail by Te Raa and Dijkstra (2002; see, for example, their Fig. 14), and we call it of Type II.

The zonally averaged snapshots for one half of the oscillation cycle are shown in Fig. 11. In a broad sense the evolution of meridional overturning (left panels) and temperature (right panels) is similar to that shown in Fig. 5, especially for the temperature, but significant differences do arise. In particular, to the north of 60 N, a pair of anomalous overturning cells of opposite sign evolves, which are not present in Fig. 5. The southern cell of this pair is near the location of maximum climatological overturning and so it actually determines the time series of Fig. 10a. In the southern part of the basin, two-to-three cells with alternating signs appear, as described by Te Raa and Dijkstra (2002, Fig. 16). The zonally averaged temperature structure also has a larger-amplitude, basin-wide signature compared to the Type-I oscillation depicted in Fig. 5.

Fig. 10

Fig. 11

This difference is seen more clearly in the evolution of depth-averaged temperatures shown in Fig. 12. The temperature anomalies in both the upper and lower layers propagate westward along the internal boundary layer determined roughly by the location of the sea-ice edge. This is in contrast with the stationary upper-layer pattern of Fig. 6 and qualitatively similar to the evolution described by Te Raa and Dijkstra (2002, Fig. 6).

Fig. 12

Huck et al. (1999) have also found two types of interdecadal oscillations in their model: one is characterized by a standing temperature anomaly in the northwestern corner of the basin, the other by temperature disturbances propagating westward along the northern boundary. They concluded that baroclinic energy conversion is crucial for either oscillation type, although the length scale of the resulting waves exceeds by far the Rossby radius of deformation. Huck and colleagues argue that the “standing” or “propagating” surface signature is selected by the degree of zonality of the surface heat-flux forcing, with more zonally uniform fluxes leading to propagating modes.

Both types of oscillations exist in our ocean–atmosphere–sea-ice model. We conclude, therefore, that neither mode depends crucially on sea-ice feedbacks, and that both are only modified in certain quantitative details by the inclusion of the sea ice.

7. Concluding remarks

a. Summary

We have studied interdecadal climate variability in an idealized hybrid coupled model of the ocean, atmosphere, and sea ice. The ocean model is a 3-D primitive-equation model on a β -plane, the atmospheric model is a 2-D EBM model of Budyko-Sellers-North type, and the sea-ice model is purely thermodynamic. We have investigated a wide range of sea-ice-related parameters, as well as explored the effect of oceanic and atmospheric parameters to which sea ice is likely to be sensitive. Over the range of parameter studied (see Table 1), the model produces a fairly realistic climatology (Figs. 1, 2), and has a reasonable ratio between meridional heat transport by the ocean and the atmosphere (Fig. 3). The sea-ice edge gives rise to an internal boundary layer in the ocean model’s main thermocline (not shown).

The modeled climate variability is most sensitive to the parameter K_{O-I} that governs the

ocean–sea-ice heat exchange. At low values of K_{O-I} , self-sustained interdecadal oscillations arise provided that the ocean’s vertical diffusivity K_V is sufficiently high (Figs. 4–6). For other parameters, this oscillation is weakly damped, with damping time scales in the range of 10 to a few hundred years. The period of the oscillation is always in the interdecadal range, that is, 30–100 years (Fig. 7). The effect of K_{O-I} in this model is similar to that of the ocean–atmosphere coupling coefficient K_{O-A} in models that do not include sea ice: increased coupling leads to shorter periods and increased damping.

We have found two types of interdecadal oscillations that differ by their surface signature. The first type is characterized by a northward-propagating temperature pattern in the northwestern corner of the ocean basin, and wave-like deep-ocean temperature anomalies that propagate westward (Fig. 5). The time series of East–West and North–South upper-ocean temperature differences are in phase opposition, with the East–West temperature difference leading and North–South temperature difference lagging the maximum meridional overturning time series by a quarter of a period (Fig. 4). The second type involves larger-scale upper-ocean temperature anomalies that propagate westward along the sea-ice edge. Westward propagation is also seen in the deep layers. For this oscillation, the East–West temperature difference is in phase opposition with the maximum meridional overturning and leads the North–South temperature difference by a quarter of a period (Figs. 10–12).

Both types of oscillations have been found previously in models without sea ice (Huck et al. 1999). The first type has been studied by Chen (1995), Chen and Ghil (1995, 1996), Greatbatch and Zhang (1995), and Huck et al. (2001). The second type has been mentioned by Huck et al. (1999), and has been extensively studied by Te Raa and Dijkstra (2002). Thus, neither oscillation type depends on the presence of sea ice and the inclusion of sea-ice processes in the model modifies either oscillation but little.

For some parameter values, the interdecadal oscillations are self-sustained, while for others they are damped. The damping time scale in the latter case is sufficiently long for the oscillations to be maintained by stochastic atmospheric forcing (Griffies and Tziperman 1995; Delworth and Greatbatch 2000). Delworth and Mann (2002) documented this type of variability in their global coupled GCM. Our analysis explains these results in greater depth and detail.

When stochastic atmospheric forcing is applied to the model, statistically significant interdecadal signals do arise in the time series of model simulations (Figs. 7 and 8). In many cases, however, the periods of these signals do not closely match those expected from the linear stability analysis of the deterministic model's equations. This happens due to modifications of climatological convective activity by the large-amplitude stochastic forcing. The random character of this forcing tends to reduce the time-mean convective activity (Fig. 9). Linear stability analysis of the system using this new climatology as a basic state predicts longer periods for the main interdecadal oscillation and matches some of the signals in the time series of the oceanic heat transport better than the linear stability analysis using the deterministic steady state. The actual periods of interdecadal variability in the stochastically forced model are bracketed, from below and above, by the results of the linear stability analyses using the steady state and stochastic climatology as the basic state, respectively (see Fig. 7).

b. Discussion

In our experiments, the wind forcing has been kept constant in time. The coupled modes of Cessi (2000) and Gallego and Cessi (2000, 2001) rely on feedback between atmospheric winds and varying SSTs; they are, therefore, not present in our model. A coupled oscillation of this type can be conceptualized as due to a delayed oscillator excited by atmospheric forcing, with the delay mechanism provided by ocean dynamics. Marshall et al. (2000) discuss various such mechanisms, one of which is associated with a decadal THC loop like that obtained in our model. Of the two types of interdecadal oscillations we find, the second type is more likely to affect atmospheric dynamics and lead to a partially coupled mode, because the SST anomalies in this oscillation have larger scale than in the other. It would be interesting to see if the oscillations obtained in a coupled GCM by Grötzner et al. (1998) can be reproduced in an intermediate ocean–sea-ice model like ours coupled to an atmospheric model of Cessi–Gallego type.

We have not found the highly nonlinear relaxation oscillations studied by Chen (1995, Ch. 5) and Chen and Ghil (1997, unpublished manuscript) in a coupled model that was quite similar to ours, but differs from it in several significant details. Exploring additional parameter regimes

might reproduce these relaxation oscillations, which represent a very interesting example of rapid climate change.

We did not include a hydrologic cycle in the present model, so that ocean salinity was not dynamically active. Yang and Neelin (1993, 1997) studied a different type of THC variability that involved in a crucial way brine rejection and freshwater input due to freezing and melting of sea ice in the mechanism leading to decadal oscillations. Including freshwater feedbacks in our model is thus a priority for future studies.

Finally, our model has a flat bottom. Winton (1997) has shown that the inclusion of topography significantly affects internal variability in 3-D THC models, while Weaver et al. (1994) found that interdecadal variability in a realistic-coastline model with a flat bottom went away when realistic bottom topography was added. Huck et al. (2001) also documented the damping influence of bottom topography on interdecadal variability in models forced by a constant buoyancy flux. They found, however, that the associated damping rates are weak, so that interdecadal oscillations are likely to still be excited by the type of stochastic atmospheric input considered in our study.

Spall and Pickart (2001) compared the time-mean circulation and the distribution of convection in two primitive-equation models: one whose bottom topography steeply slopes toward the horizontal boundaries of the sectorial model basin, the other having a flat bottom. They found significant differences between the two model versions, with the former producing results that agree better with the observations of Talley and McCartney (1982) on water mass distribution in the subpolar gyre of the North Atlantic and the Labrador Sea. Based on the sensitivity of our model's interdecadal variability to climatological convection distribution, we thus expect that, at the least, the periods of interdecadal eigenmodes will be affected by the inclusion of steep continental slopes in the model. We plan to explore the associated effects in a future study.

Acknowledgements. It is a pleasure to thank Drs. F. Chen and A. W. Robertson for help with getting started on this project. Dr. T. Huck and an anonymous reviewer provided comments that helped improve the presentation. The completion of this project was supported by NSF grant ATM00-82131 (MG) and DOE grant DE-FG-03-01ER63260 (SK).

References

- Allen, R. M., and L. A. Smith, 1996: Monte Carlo SSA: Detecting irregular oscillations in the presence of colored noise. *J. Climate*, **9**, 3373–3404.
- Arakawa, A., 1966: Computational design for long-term numerical integration of the equations of atmospheric motion. *J. Comput. Phys.*, **1**, 119–143.
- Bryan, F., 1987: Parameter sensitivity of primitive equation ocean general circulation models. *J. Phys. Oceanogr.*, **17**, 970–985.
- Bryan, K., 1969: Climate and the ocean circulation: III. The ocean model. *Mon. Wea. Rev.*, **97**, 806–827.
- Bryden, H., D. H. Roemmich, and J. A. Church, 1991: Ocean heat transport across 24°N in the Pacific. *Deep-Sea Res.*, **38**, 297–324.
- Budyko, M. I., 1969: The effect of solar radiation variations on the climate of the Earth. *Tellus*, **21**, 611–619.
- Cai, W., 1995: Interdecadal variability driven by mismatch between surface flux forcing and oceanic freshwater/heat transport. *J. Phys. Oceanogr.*, **25**, 2643–2666.
- Cai, W., 1996: The stability of NADWF under mixed boundary conditions with an improved diagnosed freshwater flux. *J. Phys. Oceanogr.*, **26**, 1081–1087.
- Cai, W., R. J. Greatbatch and S. Zhang, 1995: Interdecadal variability in an ocean model driven by a small, zonal redistribution of the surface buoyancy flux. *J. Phys. Oceanogr.*, **25**, 1998–2010.
- Capotondi, A., and R. Saravanan, 1996: Sensitivity of the thermohaline circulation to surface buoyancy forcing in a two-dimensional ocean model. *J. Phys. Oceanogr.*, **26**, 1039–1058.
- Cessi, P., 2000: Thermal feedback on wind stress as a contributing cause of climate variability. *J. Climate*, **13**, 232–244.
- Chen, F., 1995: *Coupled Ocean–Atmosphere–Sea-Ice Models of Interdecadal Variability*. Ph. D. Thesis, UCLA.
- Chen, F., and M. Ghil, 1995: Interdecadal variability of the thermohaline circulation and high latitude surface fluxes. *J. Phys. Oceanogr.*, **25**, 2547–2568.
- Chen, F., and M. Ghil, 1996: Interdecadal variability in a hybrid coupled ocean–atmosphere model. *J. Phys. Oceanogr.*, **26**, 1561–1578.
- Colin de Verdière, A., and T. Huck, 1999: Baroclinic instability: An oceanic wavemaker for interdecadal variability. *J. Phys. Oceanogr.*, **29**, 893–910.
- Delworth, T., and R. J. Greatbatch, 2000: Multidecadal thermohaline circulation variability excited by stochastic surface flux forcing. *J. Climate*, **13**, 1481–1495.

- Delworth, T., and M. E. Mann, 2000: Observed and simulated multidecadal variability in the North Atlantic. *Climate Dyn.*, **16**, 661–676.
- Delworth, T., S. Manabe, R. J. Stouffer, 1993: Interdecadal variations of the thermohaline circulation in a coupled ocean-atmosphere model. *J. Climate*, **6**, 1993–2011.
- Dettinger, M. D., M. Ghil, C. M. Strong, W. Weibel, and P. Yiou, 1995: Software expedites singular-spectrum analysis of noisy time series. *Eos, Trans. AGU*, **76**, pp. 12, 14, 21.
- Fanning, A. F., and A. J. Weaver, 1998: Thermohaline variability: The effects of horizontal resolution and diffusion. *J. Climate*, **11**, 709–715.
- Gallego, B., and P. Cessi, 2000: Exchange of heat and momentum between the atmosphere and the ocean: A minimal model of decadal oscillations. *Climate Dyn.*, **16**, 479–489.
- Gallego, B., and P. Cessi, 2001: Decadal variability of two oceans and an atmosphere. *J. Climate*, **14**, 2815–2832.
- Ghil, M., 2001: Hilbert problems for the geosciences in the 21st century. *Nonlin. Proc. Geophys.*, **8**, 211–222.
- Ghil, M., 2002: Natural climate variability. In *Encyclopedia of Global Environmental Change*, T. Munn (Ed.), Vol. 1, J. Wiley & Sons, Chichester/New York, pp. 544–549.
- Ghil, M., and S. Childress, 1987: *Topics in Geophysical Fluid Dynamics: Atmospheric Dynamics, Dynamo Theory and Climate Dynamics*. Springer-Verlag, New York/Berlin/London/Paris/Tokyo, 485 pp.
- Ghil, M., and K. C. Mo, 1991: Intraseasonal oscillations in the global atmosphere. Part I: Northern Hemisphere and tropics. *J. Atmos. Sci.*, **48**, 752–779.
- Ghil, M., and R. Vautard, 1991: Interdecadal oscillations and the warming trend in global temperature time series. *Nature*, **350**, 324–327.
- Ghil, M., and A. W. Robertson, 2000: Solving problems with GCMs: General Circulation Models and their role in the climate modeling hierarchy. In *General Circulation Model Development: Past, Present and Future*, D. Randall (Ed.), Academic Press, pp. 285–325.
- Ghil, M., M. R. Allen, M. D. Dettinger, K. Ide, D. Kondrashov, M. E. Mann, A. W. Robertson, A. Saunders, Y. Tian, F. Varadi, and P. Yiou, 2002: Advanced spectral methods for climatic time series. *Rev. Geophys.*, **40**, 3-1–3-41, 10.1029/2000GR000092.
- Gildor, H., and E. Tziperman, 2000: Sea ice as the glacial cycles climate switch: Role of seasonal and Milankovitch solar forcing. *Paleocean.*, **15**, 605–615.
- Gildor, H., and E. Tziperman, 2001: A sea-ice climate-switch mechanism for the 100kyr glacial cycles. *J. Geophys. Res.*, **106**, 9117–9133.
- Greatbatch, R. J., A. F. Fanning, A. D. Goulding, and S. Levitus, 1991: A diagnosis of interpentadal circulation changes in the North Atlantic. *J. Geophys. Res.*, **96**, 22,009–22,023.

- Greatbatch, R. J., K. A. Peterson, and H. Roth, 1997: Interdecadal variability in a coarse resolution model with North Atlantic bottom topography. Technical Report. Department of Oceanography, Dalhousie University, Halifax, Nova Scotia, Canada.
- Greatbatch, R. J., and S. Zhang, 1995: An interdecadal oscillation in an idealized ocean basin forced by constant heat flux. *J. Climate*, **8**, 81–91.
- Griffies, S. M., and E. Tziperman, 1995: A linear thermohaline oscillator driven by stochastic atmospheric forcing. *J. Climate*, **8**, 2440–2453.
- Grötzner, A., M. Latif, and T. P. Barnett, 1998: A decadal climate cycle in the North Atlantic Ocean as simulated by the ECHO coupled GCM. *J. Climate*, **11**, 831–847.
- Häkkinen, S., 1999: Variability of the simulated meridional heat transport in the North Atlantic for the period 1951–1993. *J. Geophys. Res.*, **104**, 10,991–11,007.
- Häkkinen, S., 2000: Decadal air–sea interaction in the North Atlantic based on observations and modeling results. *J. Climate*, **13**, 1195–1219.
- Hall, M. M., and H. Bryden, 1982: Direct estimates and mechanisms of ocean heat transport. *Deep-Sea Res.*, **29**, 339–359.
- Haney, R. L., 1971: Surface thermal boundary conditions for ocean circulation models. *J. Phys. Oceanogr.*, **1**, 241–248.
- Huck, T., and G. K. Vallis, 2001: Linear stability analysis of the three-dimensional thermally-driven ocean circulation: Application to interdecadal oscillations. *Tellus*, **53A**, 526–545.
- Huck, T., A. Colin de Verdière, and A. J. Weaver, 1999: Interdecadal variability of the thermohaline circulation in box-ocean models forced by fixed surface fluxes. *J. Phys. Oceanogr.*, **29**, 865–892.
- Huck, T., G. K. Vallis, and A. Colin de Verdière, 2001: On the robustness of the interdecadal modes of the thermohaline circulation. *J. Climate*, **14**, 940–963.
- Jayne, S. R., and J. Marotzke, 1999: A destabilizing thermohaline circulation–atmosphere–sea-ice feedback. *J. Climate*, **12**, 642–651.
- Josberger, E. G., 1987: Bottom ablation and heat-transfer coefficients from the 1983 Marginal Ice-Zone Experiments. *J. Geophys. Res.*, **92**, 7012–7016.
- Kravtsov, S. V., 1998: *Sea Ice and Climate Sensitivity*. Ph. D. Thesis, Florida State University, 259pp.
- Kravtsov, S. V., 2000: Sea ice and climate. Part II: Model climate stability to perturbations of the hydrological cycle. *J. Climate*, **13**, 463–487.
- Kravtsov, S. V., and W. K. Dewar 2003: On the role of the thermohaline advection and sea ice in glacial transitions. *J. Geophys. Res.*, **108**(C6), 3203, doi:10.1029/2002JC001439.
- Kushnir, Y., 1994: Interdecadal variations in North Atlantic sea surface temperature and associated atmospheric conditions. *J. Climate*, **7**, 141–157.

- Levitus, S., 1989a: Interpentadal variability of temperature and salinity at intermediate depths of the North Atlantic Ocean, 1970–1974 versus 1955–1959. *J. Geophys. Res.*, **94**, 6091–6131.
- Levitus, S., 1989b: Interpentadal variability of salinity in the upper 150 m of the North Atlantic Ocean, 1970–1974 versus 1955–1959. *J. Geophys. Res.*, **94**, 9679–9685.
- Lohmann, G., and R. Gerdes, 1998: Sea ice effects on the sensitivity of the thermohaline circulation. *J. Climate*, **11**, 2789–2803.
- Macdonald, A., C. Wunsch, 1996: An estimate of global ocean circulation and heat fluxes. *Nature*, **382**, 436–439.
- Marshall, J., H. Johnson, and J. Goodman, 2000: A study of the interaction of the North Atlantic Oscillation with ocean circulation. *J. Climate*, **14**, 1399–1421.
- Maykut, G. A., 1986: The surface heat and mass balance. *Geophysics of Sea Ice*, N. Untersteiner, Ed., Plenum Press, 395–464.
- McPhee, M. G., 1992: Turbulent heat flux in the upper ocean under sea ice. *J. Geophys. Res.*, **87**, 1550–1575.
- Molemaker, M. J., and J. C. McWilliams, 2003: Decadal modes of the thermohaline circulation. Submitted.
- Moron, V., R. Vautard, and M. Ghil, 1998: Trends, interdecadal and interannual oscillations in global sea-surface temperatures. *Clim. Dyn.*, **14**, 545–569.
- National Research Council, 1995: *Natural Climate Variability on Decade-to-Century Time Scales*. D. G. Martinson, K. Bryan, M. Ghil, M. M. Hall, T. R. Karl, E. S. Sarachik, S. Sorooshian, and L. D. Talley (Eds.), National Academy Press, Washington, D.C., 630 pp.
- Neelin, J. D., M. Latif, and F.-F. Jin, 1994: Dynamics of coupled ocean–atmosphere models: the tropical problem. *Ann. Rev. Fluid Mech*, **26**, 617–659.
- North, G. R., R. F. Cahalan, and J. A. Coakley Jr., 1981: Energy balance climate models. *Rev. Geophys. Space Phys.*, **19**, 91–121.
- Panel on Climate Variability on Decade-to-Century Time Scales (D. G. Martinson, D. S. Battisti, R. S. Bradley, J. E. Cole, R. A. Fine, M. Ghil et al.), NRC 1998: *Decade-to-Century-Scale Climate Variability and Change: A Scientific Strategy*, National Academy Press, Washington, D. C., 160 pp.
- Pacanowski, R. C., 1996: *MOM2 version 2.0 (beta) Documentation User’s Guide and Reference Manual*. Tech. Rep. 3.2, GFDL Ocean Group, 232 pp. [Available from NOAA/Geophysical Fluid Dynamics Laboratory, Princeton, NJ 08542].
- Pierce, D. W., K.-Y. Kim, T. P. Barnett, 1996: Variability of the thermohaline circulation in an ocean general circulation model coupled to an atmospheric energy balance model. *J. Phys. Oceanogr.*, **26**, 725–738.

- Saravanan, R., and J. C. McWilliams, 1998: Advective ocean–atmosphere interaction: An analytical stochastic model with implications for decadal variability. *J. Climate*, **11**, 165–188.
- Saravanan, R., G. Danabasoglu, S. C. Doney, and J. C. McWilliams, 2000: Decadal variability and predictability in midlatitude ocean–atmosphere system. *J. Climate*, **13**, 1073–1097.
- Sellers, W. D., 1969: A climate model based on the energy balance of the earth–atmosphere system. *J. Appl. Meteor.*, **8**, 392–400.
- Semtner, A. J., Jr., 1976: A model for the thermodynamic growth of sea ice in numerical investigations of climate. *J. Phys. Oceanogr.*, **6**, 379–389.
- Spall, M. A., and R. S. Pickart, 2001: Where does dense water sink? A subpolar gyre example. *J. Phys. Oceanogr.*, **31**, 810–826.
- Stephens, G. L., G. G. Campbell, and T. H. Vonder Haar, 1981: Earth radiation budgets. *J. Geophys. Res.*, **86**, 9,739–9,760.
- Talley, L. D., and M. S. McCartney, 1982: Distribution and circulation of Labrador Sea water. *J. Phys. Oceanogr.*, **12**, 1189–1205.
- Te Raa, L. A., and H. A. Dijkstra, 2002: Instability of the thermohaline circulation on interdecadal time scales. *J. Phys. Oceanogr.*, **32**, 138–160.
- Trenberth, K. E., and J. M. Caron, 2001: Estimates of meridional atmosphere and ocean heat transports. *J. Climate*, **14**, 3433–3443.
- Vautard, R., and M. Ghil, 1989: Singular spectrum analysis in nonlinear dynamics, with applications to paleoclimatic time series. *Physica D*, **35**, 395–424.
- Vautard, R., P. Yiou, and M. Ghil, 1992: Singular-spectrum analysis: A toolkit for short, noisy chaotic signals. *Physica D*, **58**, 95–126.
- Wang, W.-C., and P. H. Stone, 1980: Effect of ice–albedo feedback on global sensitivity in a one-dimensional radiative-convective climate model. *J. Atmos. Sci.*, **37**, 545–552.
- Weaver, A. J., 1995: Decadal-millennial internal ocean variability in coarse resolution ocean general circulation models. *Natural Climate Variability on Decade-to-Century Time Scales*, D. Martinson and Coeditors, Eds., National Academy Press.
- Weaver, A. J., J. Marotzke, P. F. Cummins, and E. S. Sarachik, 1993: Stability and variability of the thermohaline circulation. *J. Phys. Oceanogr.*, **23**, 39–60.
- Weaver, A. J., and E. S. Sarachik, 1991a: Evidence for decadal variability in an ocean general circulation model: an advective mechanism. *Atmos. Ocean*, **29**(2), 197–231.
- Weaver, A. J., and E. S. Sarachik, 1991b: The role of mixed boundary conditions in numerical models of the oceans climate. *J. Phys. Oceanogr.*, **21**, 1470–1493.
- Weaver, A. J., E. S. Sarachik and J. Marotzke, 1991: Freshwater flux forcing of decadal and interdecadal oceanic variability. *Nature*, **353**, 836–838.

- Weaver, A. J., S. M. Aura, and P. G. Myers, 1994: Interdecadal variability in an idealized model of the North Atlantic. *J. Geophys. Res.*, **99**, 12,423–12,441.
- Willmott, A. J., and L. A. Mysak, 1989: A simple steady-state coupled ice–ocean model, with application to the Greenland–Norwegian Sea. *J. Phys. Oceanogr.*, **19**, 501–518.
- Winton, M., 1997: The damping effect of bottom topography on internal decadal-scale oscillations of the thermohaline circulation. *J. Phys. Oceanogr.*, **27**, 203–208.
- Wood, R. G., and L. A. Mysak, 1989: A simple ice–ocean model for the Greenland Sea. *J. Phys. Oceanogr.*, **19**, 1865–1880.
- Yin, F. L., and E. S. Sarachik, 1995: Interdecadal thermohaline oscillations in a sector ocean general circulation model: advective and convective processes. *J. Phys. Oceanogr.*, **25**, 2465–2484.
- Yang, J., and J. D. Neelin, 1993: Sea-ice interaction with the thermohaline circulation. *Geophys. Res. Lett.*, **20**, 217–220.
- Yang, J., and J. D. Neelin, 1997: Decadal variability in coupled sea-ice–thermohaline circulation systems. *J. Climate*, **10**, 3059–3076.
- Zhang, S., R. J. Greatbatch, and C. A. Lin, 1993: A reexamination of the polar halocline catastrophe and implications for coupled ocean-atmosphere modeling. *J. Phys. Oceanogr.*, **23**, 287–299.
- Zhang, S., C. A. Lin, and R. J. Greatbatch, 1995: A decadal oscillation due to coupling between an ocean circulation model and a thermodynamic sea–ice model. *J. Mar. Res.*, **53**, 79–106.

TABLE 1. Model parameters. The values of Δa are nondimensional, those of K_{O-I} and K_{A-I} are in $\text{W m}^{-2}\text{C}^{-1}$, and those of K_V and D are in m^2s^{-1} . The most realistic set of parameters is in bold font.

Δa	0	0.1	0.2	
K_{O-I}	5	15	50	180
K_{A-I}	5	10	24.2	30
$K_V \times 10^4$	0.5	1		
$D \times 10^{-6}$	2	2.5		

Figure Captions

Fig. 1: Model climatology for the run with $K_{O-I} = 15 \text{ W m}^{-2} \text{ C}^{-1}$, $K_{A-I} = 24.2 \text{ W m}^{-2} \text{ C}^{-1}$, $K_V = 1.0 \times 10^{-4} \text{ m}^2 \text{ s}^{-1}$, and $D = 2 \times 10^6 \text{ m}^2 \text{ s}^{-1}$. (a) Atmospheric temperature ($^{\circ}\text{C}$), contour interval CI= 4, heavy solid lines mark ocean boundaries; (b) sea-ice thickness (m), CI= 0.5; (c) zonally averaged temperature ($^{\circ}\text{C}$), CI= 5, zero contour dotted; and (d) meridional overturning streamfunction (Sv), CI= 4. Negative contours dashed; in all panels, except for (c), the zero contour is not plotted.

Fig. 2: Dependencies of climatological sea-ice characteristics on model parameters. (a) Mean sea-ice thickness (m); and (b) latitude of the zonally averaged sea-ice edge, as functions of K_{O-I} ($\text{W m}^{-2} \text{ C}^{-1}$). Solid lines and \circ : $K_V = 1.0 \times 10^{-4} \text{ m}^2 \text{ s}^{-1}$, $D = 2.5 \times 10^6 \text{ m}^2 \text{ s}^{-1}$; dashed lines and \diamond : $K_V = 1.0 \times 10^{-4} \text{ m}^2 \text{ s}^{-1}$, $D = 2.0 \times 10^6 \text{ m}^2 \text{ s}^{-1}$; dash-dotted lines and $+$: $K_V = 0.5 \times 10^{-4} \text{ m}^2 \text{ s}^{-1}$, $D = 2.5 \times 10^6 \text{ m}^2 \text{ s}^{-1}$; dotted lines and \times : $K_V = 0.5 \times 10^{-4} \text{ m}^2 \text{ s}^{-1}$, $D = 2.0 \times 10^6 \text{ m}^2 \text{ s}^{-1}$. Scatter among the same type of markers is due to dependence on K_{A-I} .

Fig. 3: Maximum oceanic advective heat transport H_O ($\max(\int_x \int_z \rho c_p v T dx dz)$, in PW) versus maximum atmospheric heat transport H_A ($\max(-\int_x \rho_a c_{p,a} h_a D(\partial T/\partial y) dx)$, in PW). Same line types and markers as in Fig. 2 are used to show sensitivity of the results to changes in model parameters. Large values of H_O correspond to large K_{O-I} .

Fig. 4: Time series of important oceanic quantities during one cycle of a 71-year-period self-sustained oscillation with $K_{O-I} = 5 \text{ W m}^{-2} \text{ C}^{-1}$, $K_{A-I} = 24.2 \text{ W m}^{-2} \text{ C}^{-1}$, $K_V = 1.0 \times 10^{-4} \text{ m}^2 \text{ s}^{-1}$, and $D = 2 \times 10^6 \text{ m}^2 \text{ s}^{-1}$. (a) Maximum meridional overturning Ψ_m (Sv); (b) solid line: difference ΔT_{E-W} ($^{\circ}\text{C}$) between eastern and western boundary depth- and latitudinally averaged temperature in the upper layer, dashed line: difference ΔT_{N-S} ($^{\circ}\text{C}$) between northern and southern boundary depth- and longitudinally averaged temperature in the upper layer. Time in years; the quantities plotted are anomalies, that is differences between the instantaneous values and the cycle average. The horizontal averaging for ΔT_{E-W} and ΔT_{N-S} is done over the row of grid points closest to each boundary.

Fig. 5: Evolution of zonally averaged quantities during half a cycle of the oscillation in Fig. 4. Left panels: meridional overturning streamfunction (Sv), CI= 0.6; right panels: temperature

(°C), $CI= 0.08$. (a) $t = 0$; (b) $t = 1/8$; (c) $t = 1/4$; and (d) $t = 3/8$. The anomalies plotted here are differences between the instantaneous field and the long-term averaged one; negative contours dashed, zero contour is not plotted. Time is expressed in fractions of the oscillation period; snapshots at $t = 1/2$ equal those at $t = 0$ with the sign reversed and are not shown.

Fig. 6: Evolution of depth-averaged quantities during half a cycle of the oscillation in Fig. 4. Left panels: temperature (°C) in the upper layer, $CI= 0.1$; right panels: temperature (°C) in the lower layer, $CI= 0.03$. The upper layer is 1000 m thick and the lower layer is 3000 m thick. Same conventions as in Fig. 5.

Fig. 7: Oscillatory-mode parameters from linear stability analysis and from full-model simulations. Open circles are for the results of the stability analysis when linearizing about the deterministic steady state: oscillation period T (years) in the left panels and inverse decay time scale $\text{Re}(\lambda)$ (year^{-1}) in the right panels, both as functions of K_{O-I} ($\text{W m}^{-2} \text{C}^{-1}$). In the left panels x-symbols mark periods of leading significant SSA modes for 2000-year-long time series of maximum meridional heat transport by oceanic advection, from stochastically forced integrations of the full model (see text of section 6). Open triangles in the left and right panels represent the stability analysis results for the system of equations linearized about the time-mean states of stochastically forced integrations. (a) Results for $K_V = 1.0 \times 10^{-4} \text{ m}^2 \text{ s}^{-1}$, $D = 2 \times 10^6 \text{ m}^2 \text{ s}^{-1}$; (b) results for $K_V = 1.0 \times 10^{-4} \text{ m}^2 \text{ s}^{-1}$, $D = 2.5 \times 10^6 \text{ m}^2 \text{ s}^{-1}$; (c) results for $K_V = 0.5 \times 10^{-4} \text{ m}^2 \text{ s}^{-1}$, $D = 2.0 \times 10^6 \text{ m}^2 \text{ s}^{-1}$; (d) results for $K_V = 0.5 \times 10^{-4} \text{ m}^2 \text{ s}^{-1}$, $D = 2.5 \times 10^6 \text{ m}^2 \text{ s}^{-1}$. Scatter in circles and triangles for a given K_{O-I} is due to the dependence on K_{A-I} .

Fig. 8: Singular spectrum of oceanic heat transport time series for the stochastically forced integration with $K_{O-I} = 180 \text{ W m}^{-2} \text{C}^{-1}$, $K_{A-I} = 5 \text{ W m}^{-2} \text{C}^{-1}$, $K_V = 0.5 \times 10^{-4} \text{ m}^2 \text{ s}^{-1}$, and $D = 2 \times 10^6 \text{ m}^2 \text{ s}^{-1}$. The spectrum is plotted as plus signs, whose size roughly corresponds to Ghil and Mo's (1991) ad-hoc error bars. Dashed curves represent the 2nd and 97th percentile of the chi-squared red-noise test of Allen and Smith (1996). Two oscillatory pairs are significant with respect to both this test and Vautard et al.'s (1992) test; they have periods of 54 and 83 years, respectively.

Fig. 9: Climatological convective depth (m) in the experiments with $K_{O-I} = 180 \text{ W m}^{-2} \text{C}^{-1}$, $K_{A-I} = 24.2 \text{ W m}^{-2} \text{C}^{-1}$, $K_V = 10^{-4} \text{ m}^2 \text{ s}^{-1}$, and $D = 2 \times 10^6 \text{ m}^2 \text{ s}^{-1}$ for:

(a) deterministic model; and (b) stochastically forced model; contours are 100, 200, 300, 400, 500, 1000, 2000 and 3000 m. (c) Difference between the convection-depth fields of (a) and (b); CI= 200 m.

Fig. 10: Same as in Fig. 4, but for the 54-year-period damped oscillation ($\text{Re}(\lambda) = -0.08 \text{ year}^{-1}$) detected in the linear stability analysis of Fig. 7 with $K_{\text{O-I}} = 180 \text{ W m}^{-2} \text{ C}^{-1}$, $K_{\text{A-I}} = 5 \text{ W m}^{-2} \text{ C}^{-1}$, $K_{\text{V}} = 0.5 \times 10^{-4} \text{ m}^2 \text{ s}^{-1}$, and $D = 2 \times 10^6 \text{ m}^2 \text{ s}^{-1}$. Time series are multiplied by $\exp(-\text{Re}(\lambda)t)$ and normalized to have the same amplitude of the maximum meridional overturning as for the self-sustained oscillation in Fig. 4. This oscillation appears as the leading significant SSA mode in Fig. 8.

Fig. 11: Same as in Fig. 5, but for the oscillation depicted in Fig. 10.

Fig. 12: Same as in Fig. 6, but for the oscillation depicted in Fig. 10.

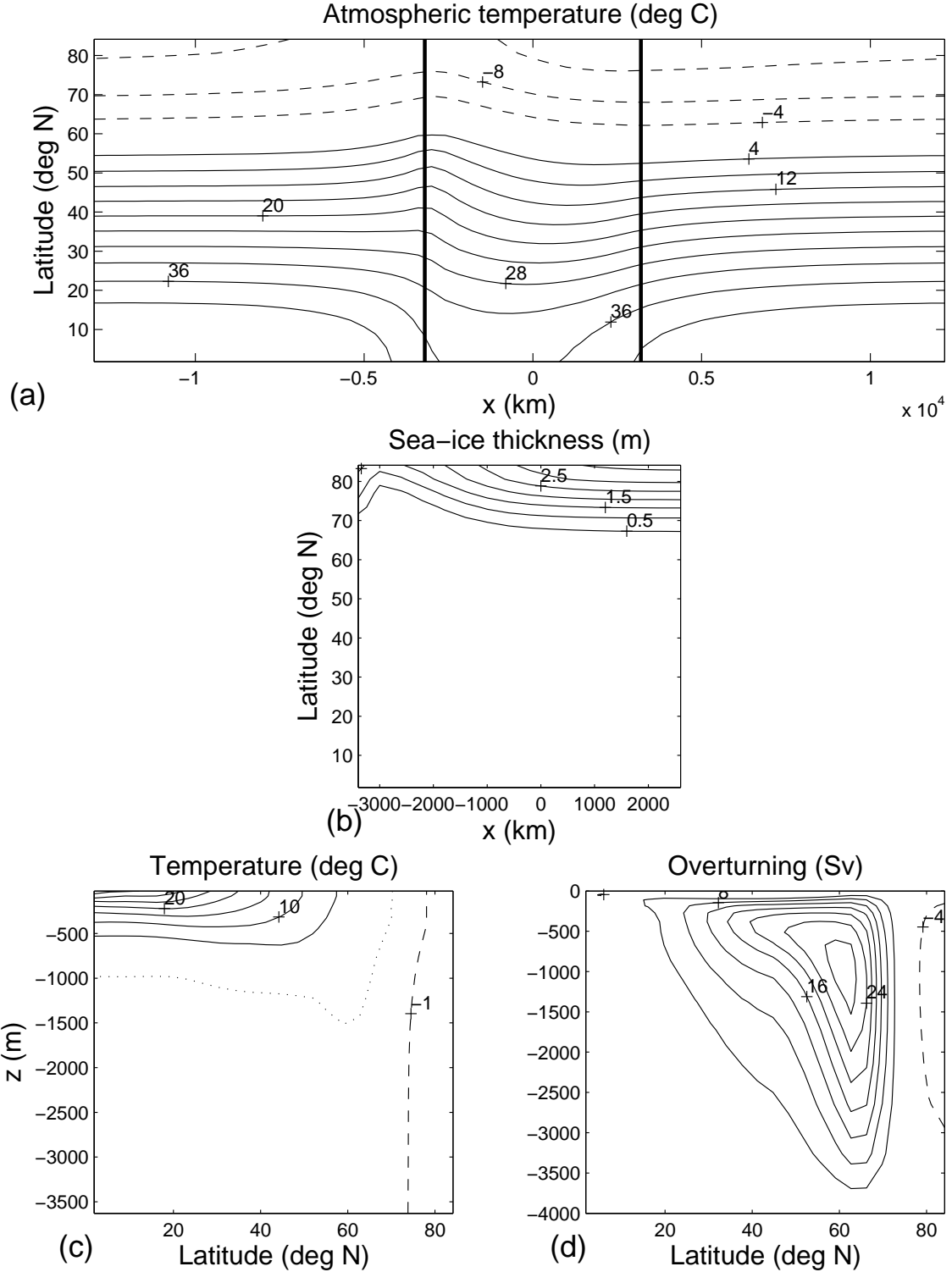


Figure 1: Model climatology for the run with $K_{O-I} = 15 \text{ W m}^{-2} \text{ C}^{-1}$, $K_{A-I} = 24.2 \text{ W m}^{-2} \text{ C}^{-1}$, $K_V = 1.0 \times 10^{-4} \text{ m}^2 \text{ s}^{-1}$, and $D = 2 \times 10^6 \text{ m}^2 \text{ s}^{-1}$. (a) Atmospheric temperature ($^{\circ}\text{C}$), contour interval $\text{CI}=4$, heavy solid lines mark ocean boundaries; (b) sea-ice thickness (m), $\text{CI}=0.5$; (c) zonally averaged temperature ($^{\circ}\text{C}$), $\text{CI}=5$, zero contour dotted; and (d) meridional overturning streamfunction (Sv), $\text{CI}=4$. Negative contours dashed; in all panels, except for (c), the zero contour is not plotted.

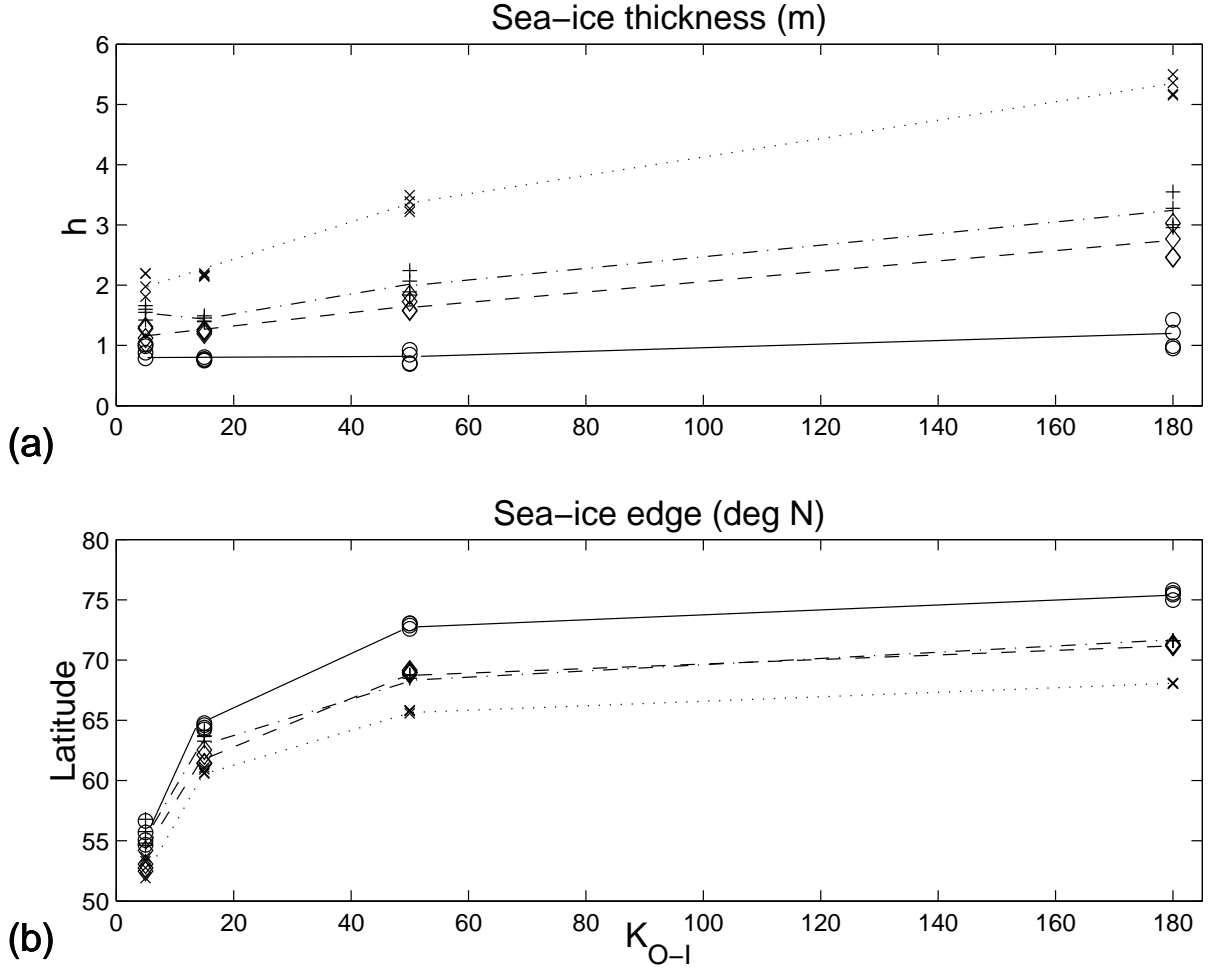


Figure 2: Dependencies of climatological sea-ice characteristics on model parameters. (a) Mean sea-ice thickness (m); and (b) latitude of the zonally averaged sea-ice edge, as functions of K_{O-I} ($\text{W m}^{-2} \text{C}^{-1}$). Solid lines and \circ : $K_V = 1.0 \times 10^{-4} \text{ m}^2 \text{s}^{-1}$, $D = 2.5 \times 10^6 \text{ m}^2 \text{s}^{-1}$; dashed lines and \diamond : $K_V = 1.0 \times 10^{-4} \text{ m}^2 \text{s}^{-1}$, $D = 2.0 \times 10^6 \text{ m}^2 \text{s}^{-1}$; dash-dotted lines and $+$: $K_V = 0.5 \times 10^{-4} \text{ m}^2 \text{s}^{-1}$, $D = 2.5 \times 10^6 \text{ m}^2 \text{s}^{-1}$; dotted lines and \times : $K_V = 0.5 \times 10^{-4} \text{ m}^2 \text{s}^{-1}$, $D = 2.0 \times 10^6 \text{ m}^2 \text{s}^{-1}$. Scatter among the same type of markers is due to dependence on K_{A-I} .

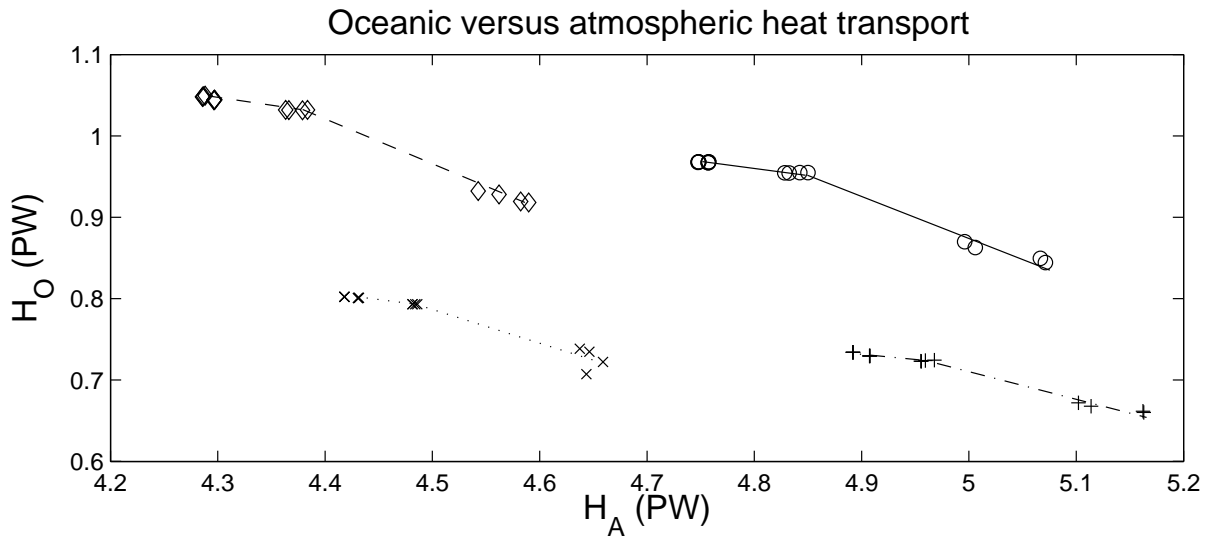


Figure 3: Maximum oceanic advective heat transport H_O ($\max(\int_x \int_z \rho c_p v T dx dz)$, in PW) versus maximum atmospheric heat transport H_A ($\max(-\int_x \rho_a c_{p,a} h_a D(\partial T/\partial y) dx)$, in PW). Same line types and markers as in Fig. 2 are used to show sensitivity of the results to changes in model parameters. Large values of H_O correspond to large K_{O-I} .

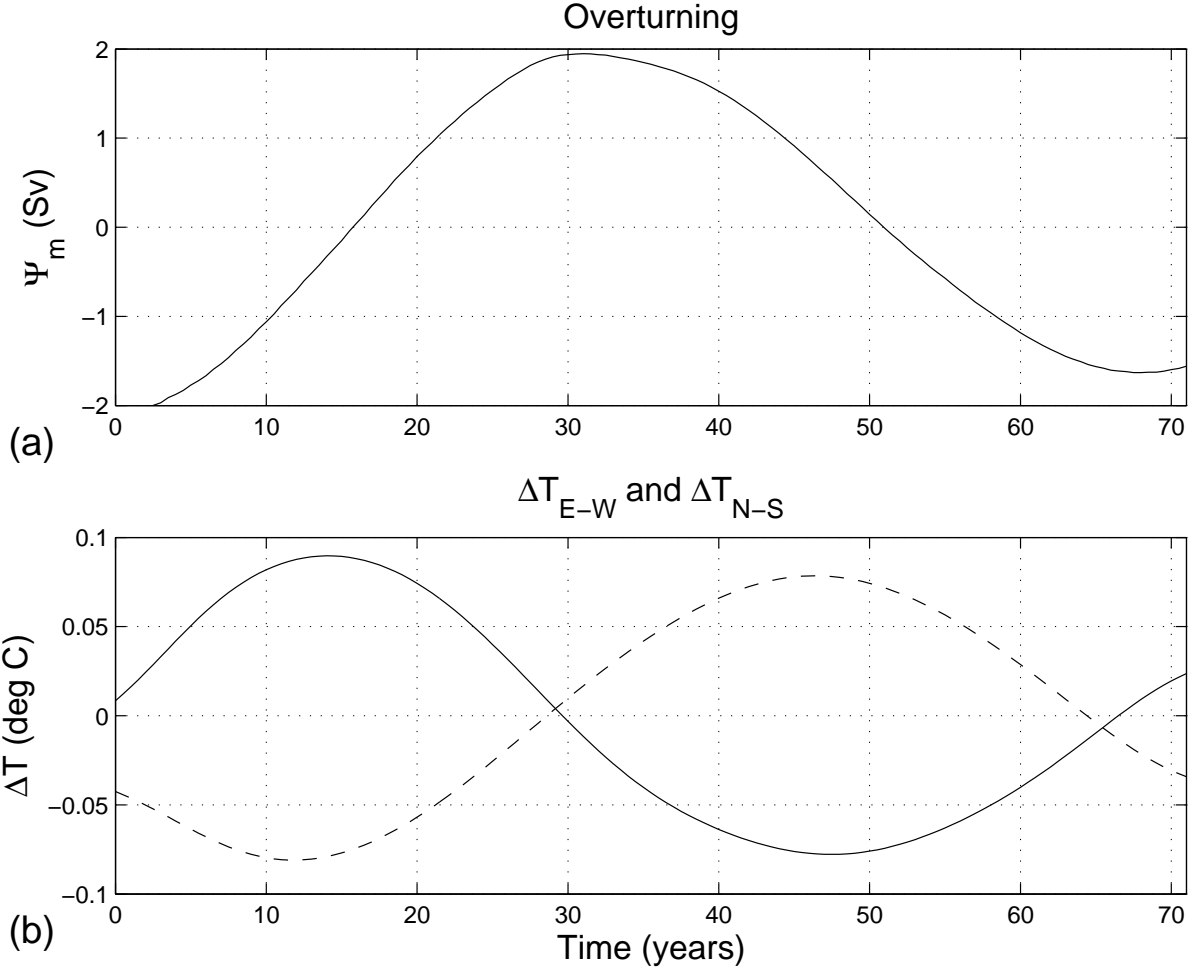


Figure 4: Time series of important oceanic quantities during one cycle of a 71-year-period self-sustained oscillation with $K_{O-I} = 5 \text{ W m}^{-2} \text{ C}^{-1}$, $K_{A-I} = 24.2 \text{ W m}^{-2} \text{ C}^{-1}$, $K_V = 1.0 \times 10^{-4} \text{ m}^2 \text{ s}^{-1}$, and $D = 2 \times 10^6 \text{ m}^2 \text{ s}^{-1}$. (a) Maximum meridional overturning Ψ_m (Sv); (b) solid line: difference ΔT_{E-W} ($^{\circ}\text{C}$) between eastern and western boundary depth- and latitudinally averaged temperature in the upper layer, dashed line: difference ΔT_{N-S} ($^{\circ}\text{C}$) between northern and southern boundary depth- and longitudinally averaged temperature in the upper layer. Time in years; the quantities plotted are anomalies, that is differences between the instantaneous values and the cycle average. The horizontal averaging for ΔT_{E-W} and ΔT_{N-S} is done over the row of grid points closest to each boundary.

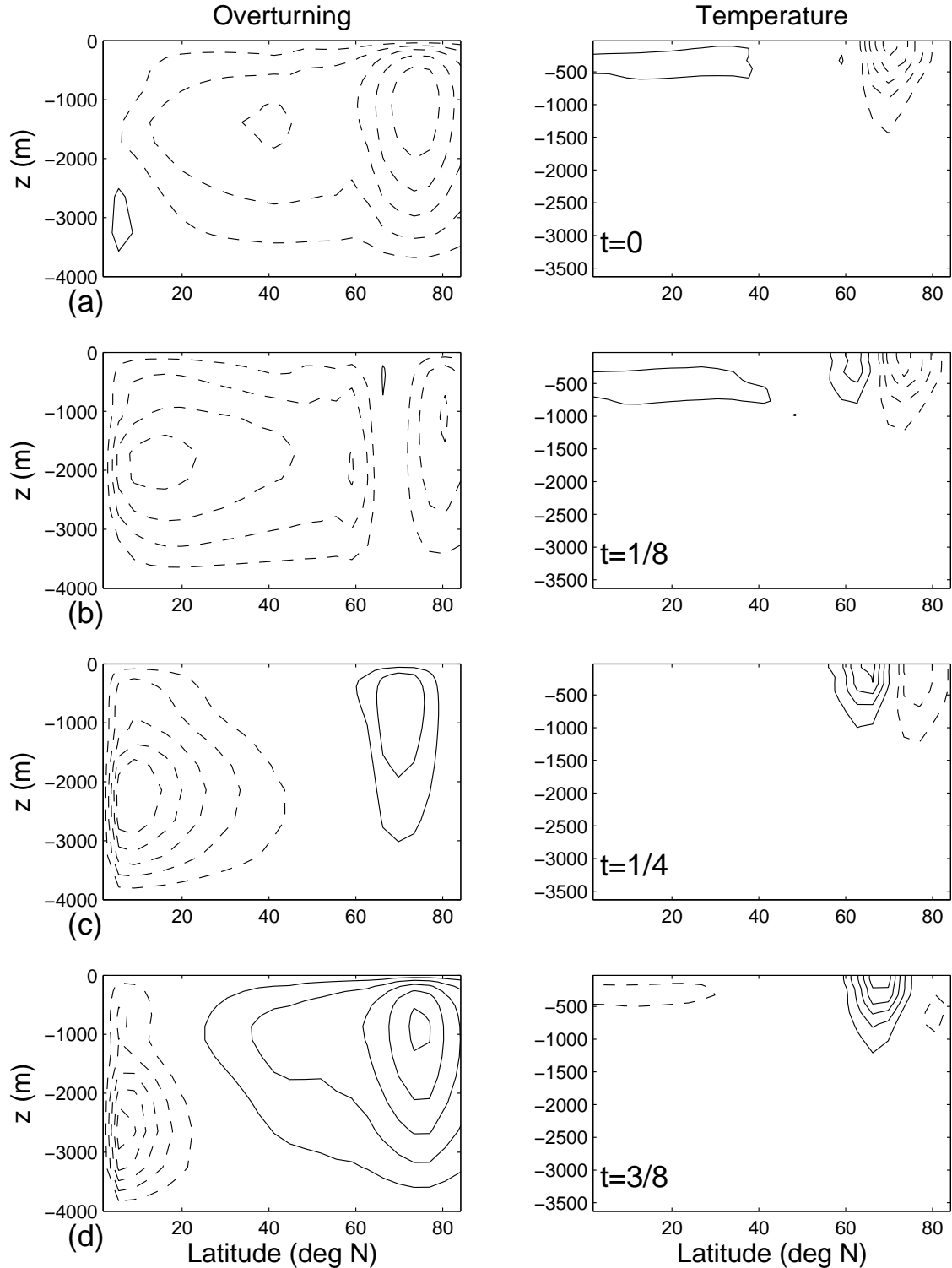


Figure 5: Evolution of zonally averaged quantities during half a cycle of the oscillation in Fig. 4. Left panels: meridional overturning streamfunction (Sv), $CI=0.6$; right panels: temperature ($^{\circ}C$), $CI=0.08$. (a) $t=0$; (b) $t=1/8$; (c) $t=1/4$; and (d) $t=3/8$. The anomalies plotted here are differences between the instantaneous field and the long-term averaged one; negative contours dashed, zero contour is not plotted. Time is expressed in fractions of the oscillation period; snapshots at $t=1/2$ equal those at $t=0$ with the sign reversed and are not shown.

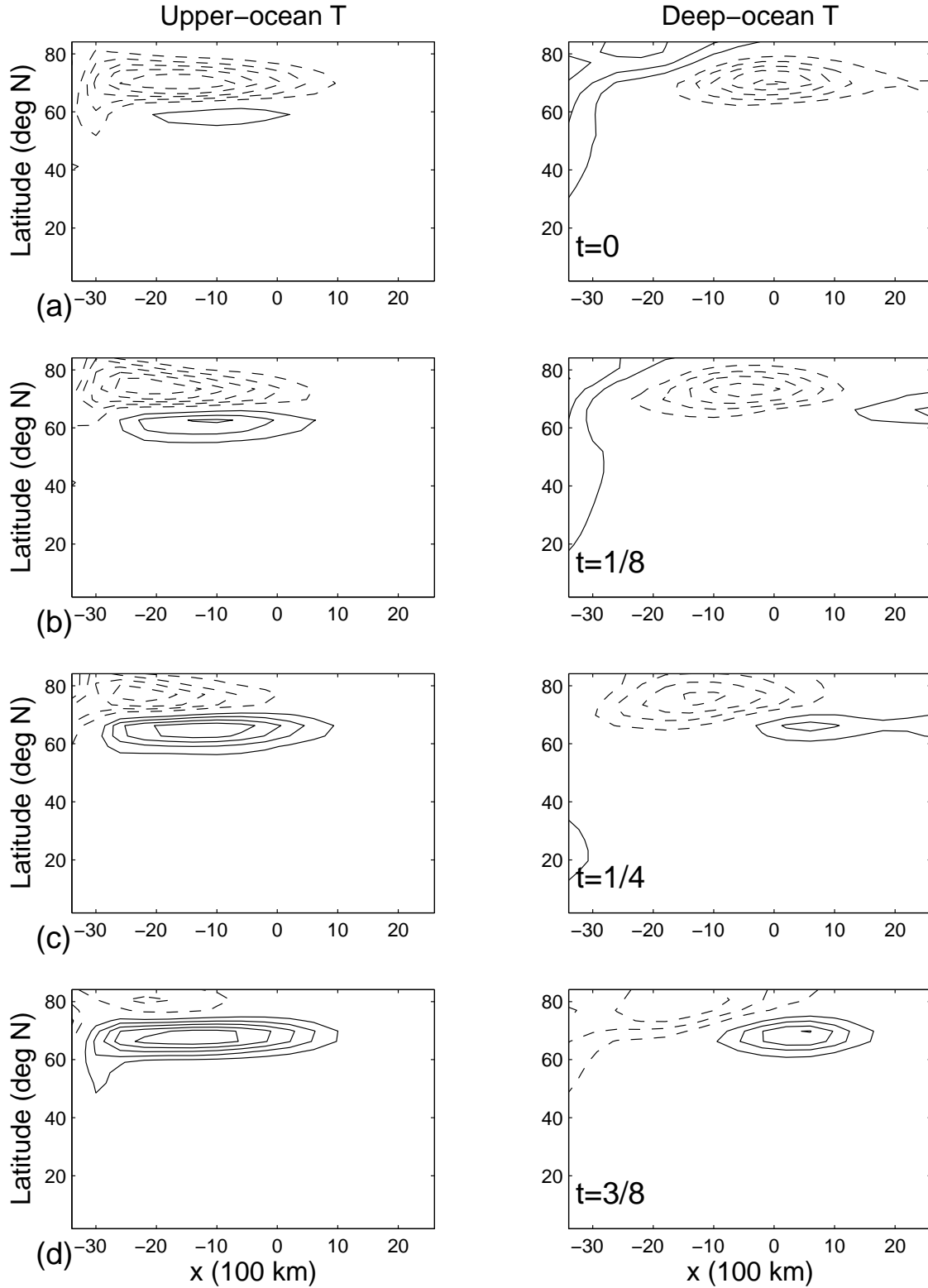


Figure 6: Evolution of depth-averaged quantities during half a cycle of the oscillation in Fig. 4. Left panels: temperature ($^{\circ}\text{C}$) in the upper layer, $\text{CI}= 0.1$; right panels: temperature ($^{\circ}\text{C}$) in the lower layer, $\text{CI}= 0.03$. The upper layer is 1000 m thick and the lower layer is 3000 m thick. Same conventions as in Fig. 5.

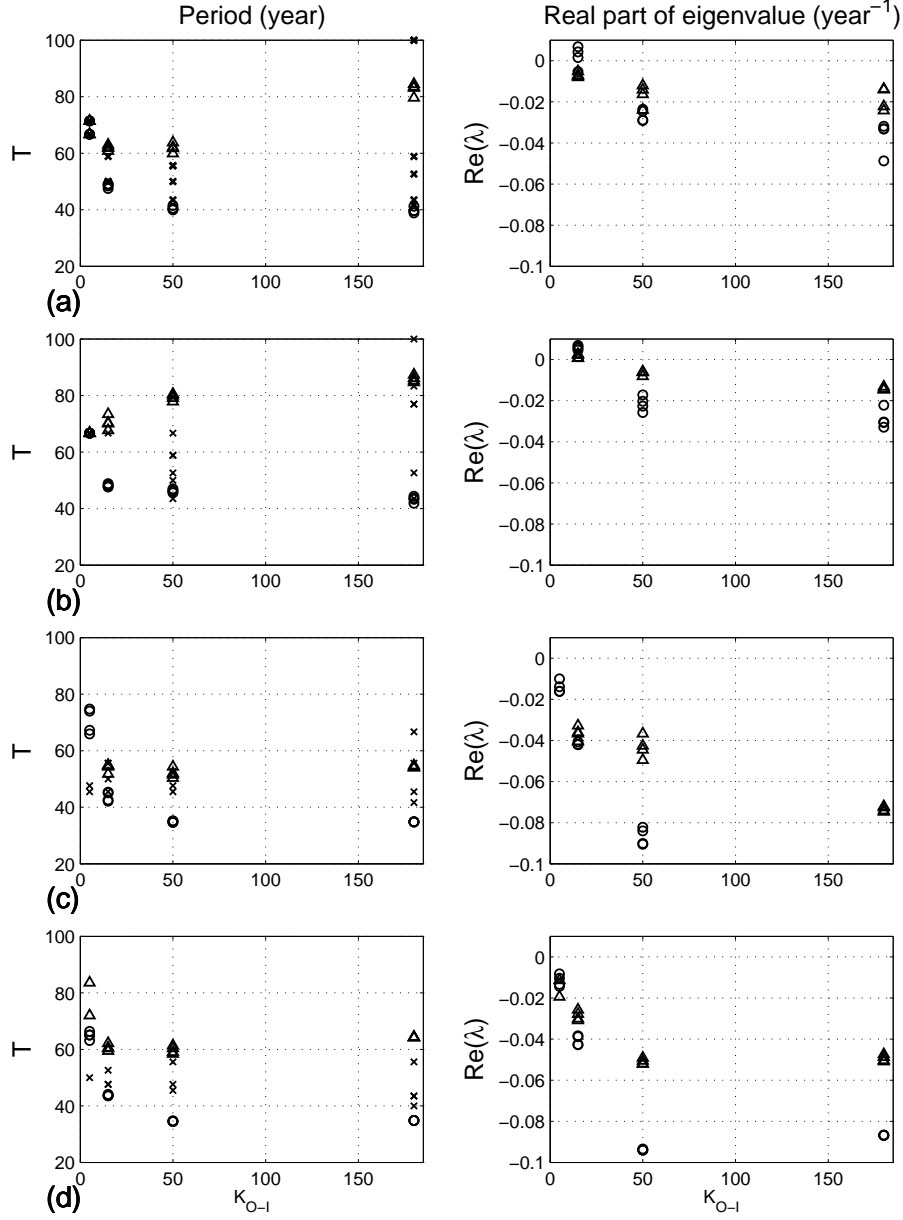


Figure 7: Oscillatory-mode parameters from linear stability analysis and from full-model simulations. Open circles are for the results of the stability analysis when linearizing about the deterministic steady state: oscillation period T (years) in the left panels and inverse decay time scale $\text{Re}(\lambda)$ (year^{-1}) in the right panels, both as functions of $K_{\text{O-I}}$ ($\text{W m}^{-2} \text{C}^{-1}$). In the left panels x-symbols mark periods of leading significant SSA modes for 2000-year-long time series of maximum meridional heat transport by oceanic advection, from stochastically forced integrations of the full model (see text of section 6). Open triangles in the left and right panels represent the stability analysis results for the system of equations linearized about the time-mean states of stochastically forced integrations. (a) Results for $K_{\text{V}} = 1.0 \times 10^{-4} \text{ m}^2 \text{ s}^{-1}$, $D = 2 \times 10^6 \text{ m}^2 \text{ s}^{-1}$; (b) results for $K_{\text{V}} = 1.0 \times 10^{-4} \text{ m}^2 \text{ s}^{-1}$, $D = 2.5 \times 10^6 \text{ m}^2 \text{ s}^{-1}$; (c) results for $K_{\text{V}} = 0.5 \times 10^{-4} \text{ m}^2 \text{ s}^{-1}$, $D = 2.0 \times 10^6 \text{ m}^2 \text{ s}^{-1}$; (d) results for $K_{\text{V}} = 0.5 \times 10^{-4} \text{ m}^2 \text{ s}^{-1}$, $D = 2.5 \times 10^6 \text{ m}^2 \text{ s}^{-1}$. Scatter in circles and triangles for a given $K_{\text{O-I}}$ is due to the dependence on $K_{\text{A-I}}$.

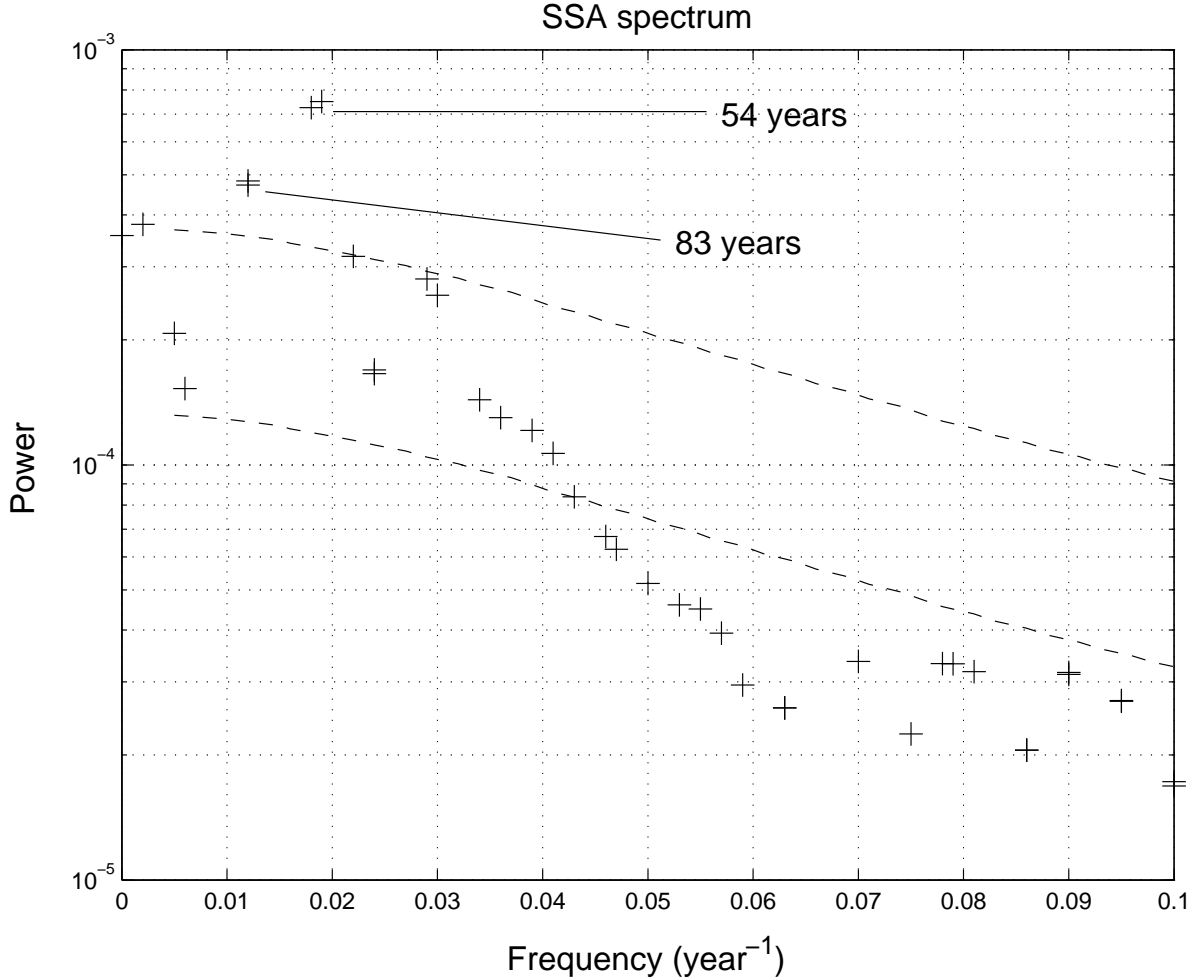


Figure 8: Singular spectrum of oceanic heat transport time series for the stochastically forced integration with $K_{O-I} = 180 \text{ W m}^{-2} \text{ C}^{-1}$, $K_{A-I} = 5 \text{ W m}^{-2} \text{ C}^{-1}$, $K_V = 0.5 \times 10^{-4} \text{ m}^2 \text{ s}^{-1}$, and $D = 2 \times 10^6 \text{ m}^2 \text{ s}^{-1}$. The spectrum is plotted as plus signs, whose size roughly corresponds to Ghil and Mo's (1991) ad-hoc error bars. Dashed curves represent the 2nd and 97th percentile of the chi-squared red-noise test of Allen and Smith (1996). Two oscillatory pairs are significant with respect to both this test and Vautard et al.'s (1992) test; they have periods of 54 and 83 years, respectively.

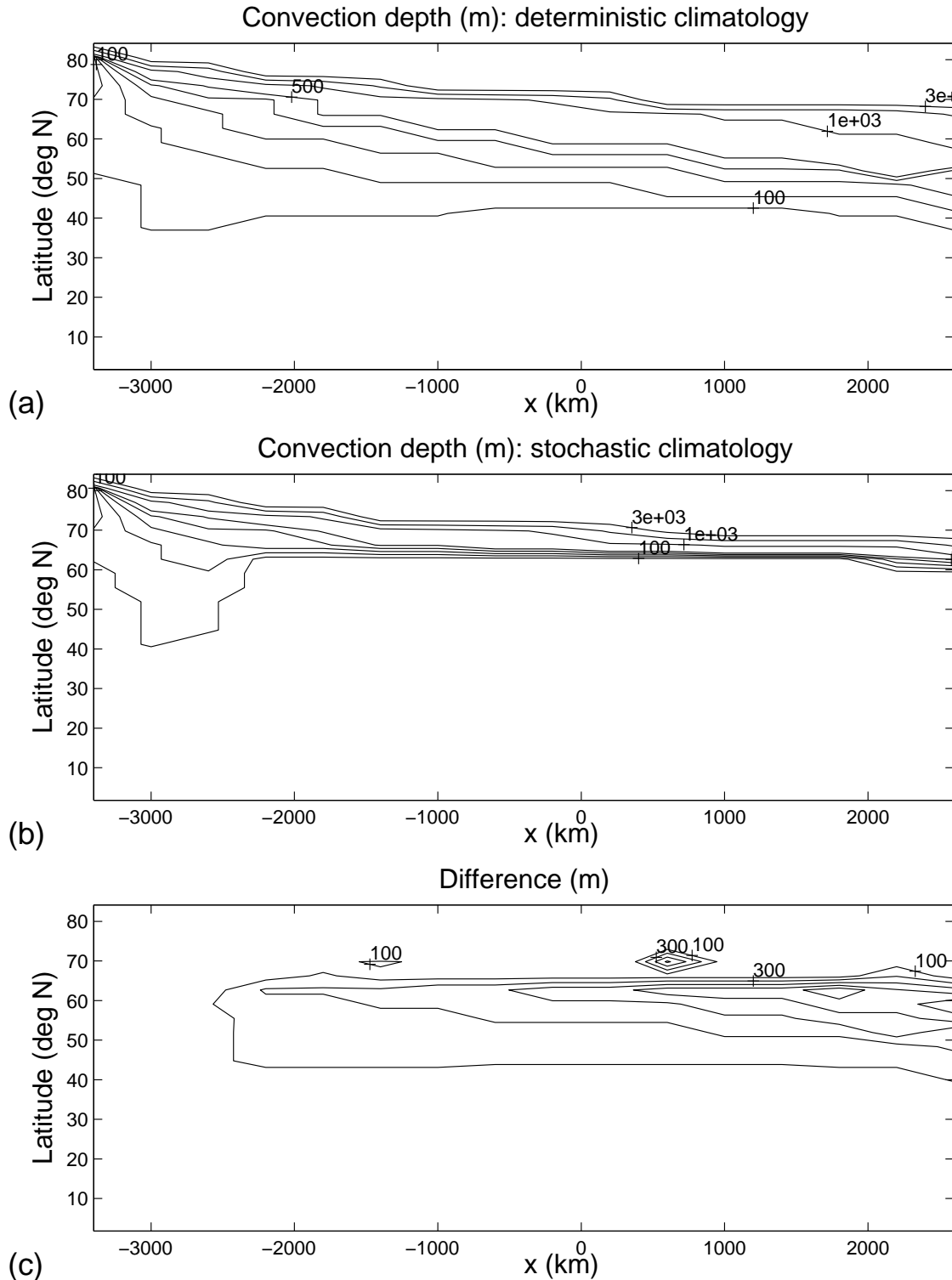


Figure 9: Climatological convective depth (m) in the experiments with $K_{O-I} = 180 \text{ W m}^{-2} \text{ C}^{-1}$, $K_{A-I} = 24.2 \text{ W m}^{-2} \text{ C}^{-1}$, $K_V = 10^{-4} \text{ m}^2 \text{ s}^{-1}$, and $D = 2 \times 10^6 \text{ m}^2 \text{ s}^{-1}$ for: (a) deterministic model; and (b) stochastically forced model; contours are 100, 200, 300, 400, 500, 1000, 2000 and 3000 m. (c) Difference between the convection-depth fields of (a) and (b); CI= 200 m.

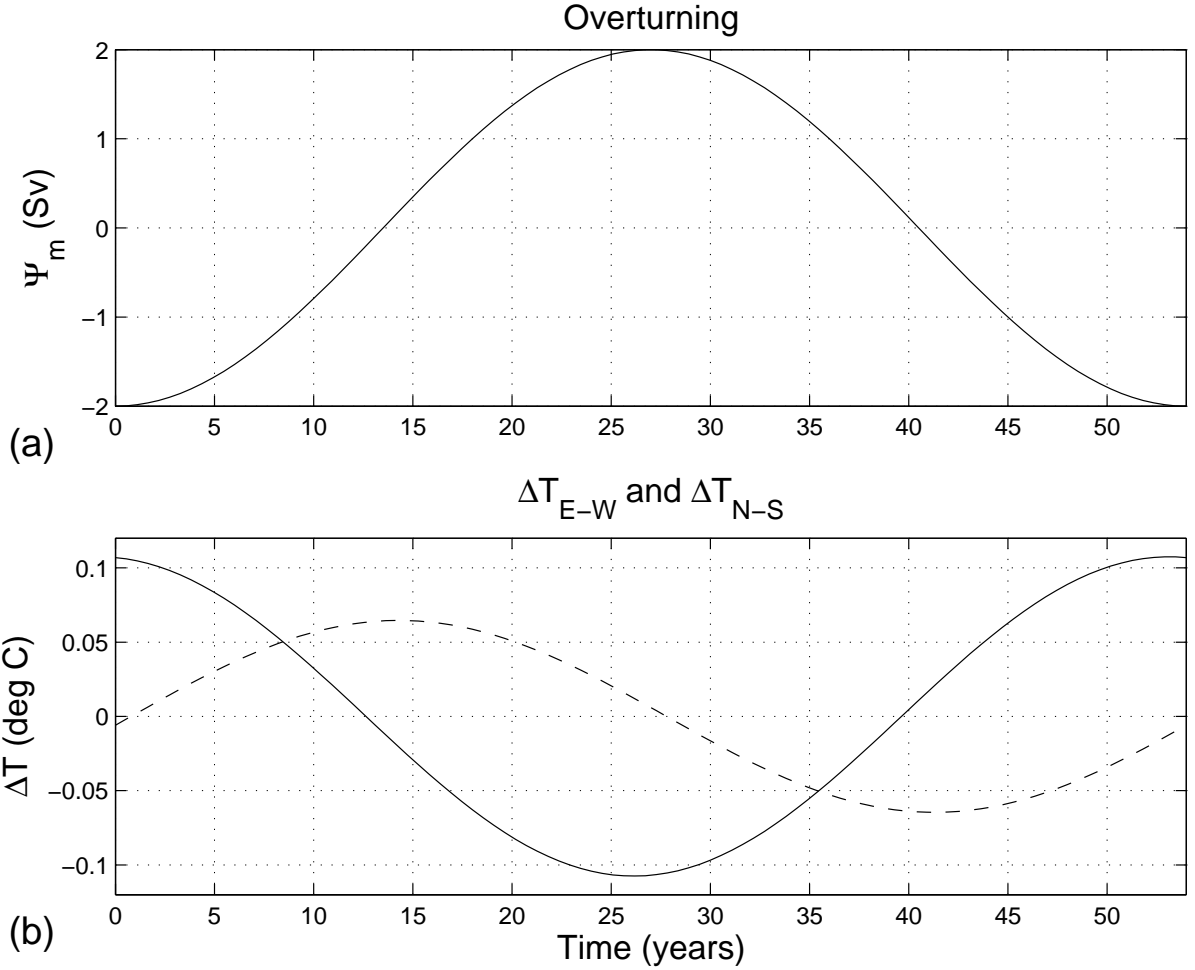


Figure 10: Same as in Fig. 4, but for the 54-year-period damped oscillation ($\text{Re}(\lambda) = -0.08 \text{ year}^{-1}$) detected in the linear stability analysis of Fig. 7 with $K_{O-I} = 180 \text{ W m}^{-2} \text{ C}^{-1}$, $K_{A-I} = 5 \text{ W m}^{-2} \text{ C}^{-1}$, $K_V = 0.5 \times 10^{-4} \text{ m}^2 \text{ s}^{-1}$, and $D = 2 \times 10^6 \text{ m}^2 \text{ s}^{-1}$. Time series are multiplied by $\exp(-\text{Re}(\lambda)t)$ and normalized to have the same amplitude of the maximum meridional overturning as for the self-sustained oscillation in Fig. 4. This oscillation appears as the leading significant SSA mode in Fig. 8.

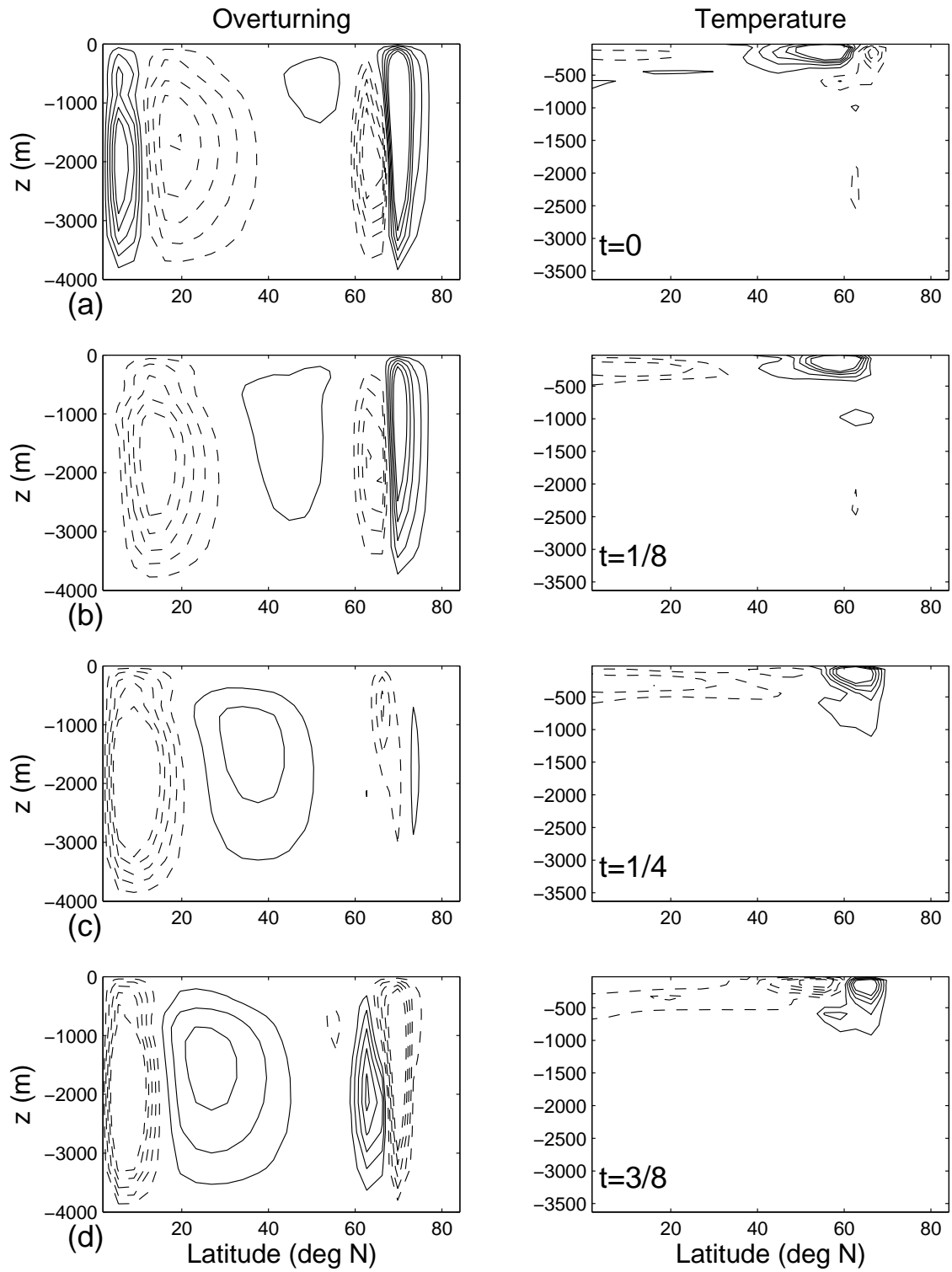


Figure 11: Same as in Fig. 5, but for the oscillation depicted in Fig. 10.

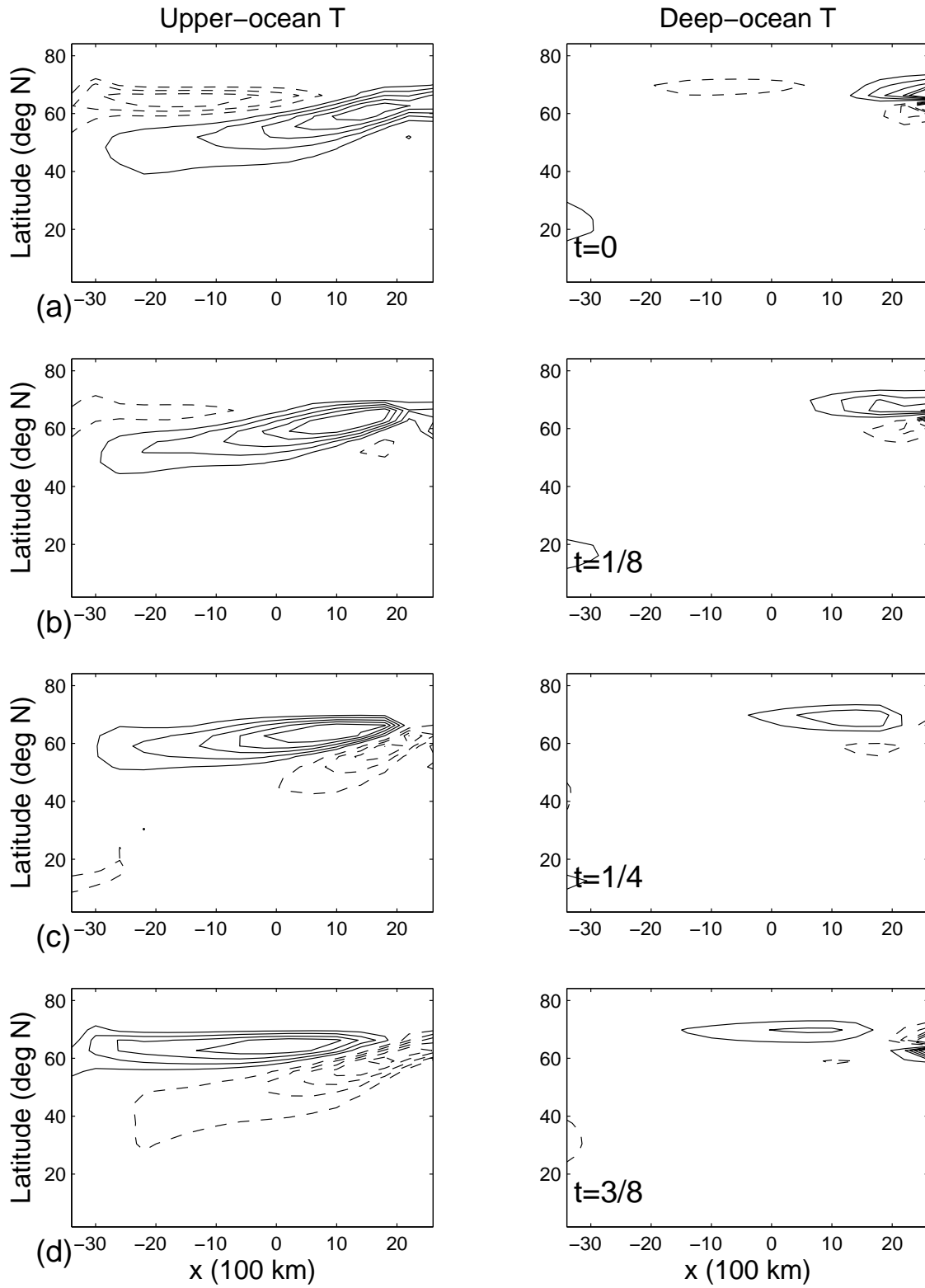


Figure 12: Same as in Fig. 6, but for the oscillation depicted in Fig. 10.